Carbon cycle responses to changes in weathering and the long-term fate of stable carbon isotopes

Aurich Jeltsch-Thömmes[1] and Fortunat Joos[1]

[1]University of Bern

December 7, 2022

Abstract

The causes of the variations in CO_2 of the past million years remain poorly understood. Imbalances between the input of elements from rock weathering and their removal from the atmosphere-ocean-biosphere system to the lithosphere likely contributed to reconstructed changes. We employ the Bern3D Earth system model of intermediate complexity to investigate carbon-climate responses to step-changes in the weathering input of phosphorus, alkalinity, carbon, and carbon isotope ratio ($\delta^{13}C$) in simulations extending up to 600,000 years.

CO_2 and climate approach a new equilibrium within a few ten thousand years, whereas the equilibration lasts several hundred thousand years for $\delta^{13}C$. These timescales represent a challenge for the initialization of sediment-enabled models and unintended drifts may be larger than forced signals in simulations of the last glacial-interglacial cycle. Changes in dissolved CO_2 change isotopic fractionation during marine photosynthesis and $\delta^{13}C$ of organic matter. This mechanism and changes in the organic matter export cause distinct spatio-temporal perturbations in $\delta^{13}C$ of dissolved inorganic carbon.

A cost-efficient emulator is built with the Bern3D responses and applied in contrasting literature-based weathering histories for the past 800,000 years. Differences between scenarios for carbonate rock weathering reach around a third of the glacial-interglacial CO_2 amplitude, 0.05 exceed reconstructed variations in marine carbonate ion. Plausible input from the decomposition of organic matter on shelves causes variations of up to 10 ppm in CO_2, 4 mmol m^{-3} in CO^{2-}_3, and 0.09$\delta^{13}C$. Our results demonstrate that weathering-burial imbalances are important for past climate variations.

Carbon cycle responses to changes in weathering and the long-term fate of stable carbon isotopes

A. Jeltsch-Thömmes and F. Joos

Climate and Environmental Physics, Physics Institute and Oeschger Centre for Climate Change Research, University of Bern, Bern, Switzerland

Key Points:

- Earth system's response to weathering changes is probed in 600,000 year-long simulations with the Bern3D model and a cost-efficient emulator
- Equilibration timescales are order 10,000 years for CO_2 and 100,000 years for $\delta^{13}C$, requiring careful model initialization
- Literature-based weathering scenarios for the past 800,000 years reveal significant responses in CO_2, carbonate ion, and $\delta^{13}C$

Corresponding author: A. Jeltsch-Thömmes, `aurich.jeltsch-thoemmes@unibe.ch`

Abstract

The causes of the variations in CO_2 of the past million years remain poorly understood. Imbalances between the input of elements from rock weathering and their removal from the atmosphere-ocean-biosphere system to the lithosphere likely contributed to reconstructed changes. We employ the Bern3D Earth system model of intermediate complexity to investigate carbon-climate responses to step-changes in the weathering input of phosphorus, alkalinity, carbon, and carbon isotope ratio (δ^{13}C) in simulations extending up to 600,000 years. CO_2 and climate approach a new equilibrium within a few ten thousand years, whereas the equilibration lasts several hundred thousand years for δ^{13}C. These timescales represent a challenge for the initialization of sediment-enabled models and unintended drifts may be larger than forced signals in simulations of the last glacial-interglacial cycle. Changes in dissolved CO_2 change isotopic fractionation during marine photosynthesis and δ^{13}C of organic matter. This mechanism and changes in the organic matter export cause distinct spatio-temporal perturbations in δ^{13}C of dissolved inorganic carbon. A cost-efficient emulator is built with the Bern3D responses and applied in contrasting literature-based weathering histories for the past 800,000 years. Differences between scenarios for carbonate rock weathering reach around a third of the glacial-interglacial CO_2 amplitude, 0.05‰ for δ^{13}C, and exceed reconstructed variations in marine carbonate ion. Plausible input from the decomposition of organic matter on shelves causes variations of up to 10 ppm in CO_2, 4 mmol m^{-3} in CO_3^{2-}, and 0.09‰ in δ^{13}C. Our results demonstrate that weathering-burial imbalances are important for past climate variations.

Plain Language Summary

Data from ice cores and marine sediments document large changes in atmospheric carbon dioxide (CO_2) and climate during the past million years. Carbon isotopes and other proxies can help to understand underlying processes. In this study, we investigate Earth's response to plausible changes in the input of carbon and other elements from the weathering of rocks or the decomposition of previously accumulated organic matter with the help of a computer model. Results show significant variations in CO_2, carbon isotopes, marine chemistry, marine biological productivity, and burial fluxes of biogenic particles to the lithosphere. The adjustment time to changes in input flux is several ten thousand years for CO_2 and climate, and several hundred thousand years for carbon isotopes. As it is computationally challenging to simulate such long time periods with complex models, we used our results to build an emulator. Such emulators, representing the responses of spatially-resolved and process-based models, are useful for studies addressing Earth's history over many millions of years. Simulating a million years with the emulator takes seconds, whereas it takes about three months with the complex model. In conclusion, our work highlights the role of weathering fluxes and their possible contribution to past climate-carbon cycle swings.

1 Introduction

Chemical weathering of rocks and deposits eventually provides a continuous flow of carbon and other elements to the ocean (e.g. Walker et al., 1981; Berner, 1990; Suchet & Probst, 1995; Hartmann et al., 2014; Compton et al., 2000; Lacroix et al., 2021), thereby influencing climate, atmospheric CO_2, carbon isotopes, biogeochemical cycles, and the oxidative capacity at the Earth's surface on millennial and longer time scales (Kump & Alley, 1994; Hayes & Waldbauer, 2006). However, Earth's system responses to changes in weathering remain uncertain and their representation in Earth system simulations extending over many thousands or even millions of years challenging.

Proxy records show climate and biogeochemical cycles to vary on orbital time scales (Lisiecki & Raymo, 2005; Lisiecki, 2014). Over the past 800 thousand years (kyr), ice

core records document past changes in atmospheric CO_2 (e.g., Neftel et al., 1982; Siegenthaler et al., 2005; Lüthi et al., 2008; Marcott et al., 2014; Bereiter et al., 2015) and in its stable carbon isotope ratio, $\delta^{13}C_{atm}$ ($^{13}C/^{12}C$ in permil units), (e.g., Lourantou et al., 2010; Schmitt et al., 2012; Schneider et al., 2013; Eggleston et al., 2016). Variations in the greenhouse gas CO_2 strongly contributed to glacial-interglacial climate swings and $\delta^{13}C$ records constrain related biogeochemical processes. Marine records of $\delta^{13}C$ (e.g., Raymo et al., 1997; Hoogakker et al., 2006; Oliver et al., 2010; Schmittner et al., 2013; Lisiecki, 2014; C. D. Peterson et al., 2014; C. D. Peterson & Lisiecki, 2018), carbonate preservation (e.g., L. C. Peterson & Prell, 1985), and other proxies reach further back in time and cover the Pleistocene epoch, although with partly sparse spatial coverage and lower temporal resolution.

Weathering fluxes enter the ocean through riverine transport in the form of dissolved inorganic and organic compounds and particulate organic matter (Meybeck, 1982; Regnier et al., 2013; Tréguer et al., 2021; Lacroix et al., 2021). For example, phosphorus is primarily delivered to the ocean as particulate organic phosphate (POP), mediated by land biosphere processes, and attached to surfaces of iron-manganese and hydroxide particles, in addition to dissolved inorganic and dissolved organic phosphorus (Compton et al., 2000; Lacroix et al., 2021). Estimates suggest that there are weathering hotspots and that 70% of today's global weathering fluxes derive from only 10% of the land area (Hartmann et al., 2014). Carbon is also released to the climate system via outgassing of magmas at seafloor hydrothermal vents, hot-spot and island arc volcanoes, and by other forms of volcanism (Hayes & Waldbauer, 2006). Chemical weathering rates are thought to be governed by lithology, hydrology and runoff, rates of physical erosion, soil properties and shielding of rocks by soils, and temperature. (e.g., Hartmann et al., 2014; Colbourn et al., 2013). All these parameters changed over glacial-interglacial cycles and Earth's history.

The input of carbon and nutrients from the lithosphere is roughly balanced by the burial of biogenic particles and other material in the lithosphere, yet imbalances remain. For example, the input by weathering and the input-burial balance was strongly perturbed over past glacial-interglacial cycles (L. C. Peterson & Prell, 1985; Broecker & Peng, 1987; Kump & Alley, 1994; Cartapanis et al., 2016, 2018). Input-burial imbalances directly affect the inventories and concentrations of carbon, nutrients, and alkalinity in the ocean. In turn, the production and burial of biogenic particles are changing.

The burial of biogenic particles is mediated by the marine carbon and biogeochemical cycles (e.g., Emerson & Bender, 1981; Sarmiento & Gruber, 2006; Tschumi et al., 2011). Marine ecosystems remove dissolved inorganic carbon (DIC), nutrients, and alkalinity from surface waters to eventually generate dissolved organic matter and particles of calcium carbonate ($CaCO_3$), opal, and organic matter. The particles sink through the water column towards the ocean floor. This biogenic material is mainly remineralized to DIC and inorganic nutrients within the water column and surface (reactive) sediments, but a fraction is buried in consolidated sediments. Rates of particle sinking, remineralization, and burial depend on particle size and composition, and environmental parameters. These parameters include, for example, temperature, oxygen, viscosity, or the saturation state of water for $CaCO_3$ in the water column and reactive sediments. Large amounts of carbon and nutrients get buried in organic forms in the coastal zone and on continental shelves (Regnier et al., 2013; Wallmann et al., 2016). This material may be released again from exposed shelves during low glacial sea level and contribute, together with changes in weathering and burial, to imbalances between fluxes from and to the lithosphere (Wallmann, 2014; Wallmann et al., 2016). Changes in surface ocean DIC and alkalinity from input-burial imbalances and altered particle cycling change atmospheric CO_2, forcing climate to change. Input-burial imbalances also strongly affect $\delta^{13}C$ of carbon in the atmosphere, ocean, ocean sediments, and the land biosphere (Broecker, 1970;

Schrag et al., 2013; Roth et al., 2014; Mills et al., 2017; Jeltsch-Thömmes & Joos, 2020; Komar & Zeebe, 2021).

Modeling the responses to input-burial imbalances is computationally challenging. The response time scales to input-burial imbalances range from several millennia to hundreds of thousands of years for CO_2 (e.g. Archer et al., 1998; Colbourn et al., 2015) and $\delta^{13}C$ (Roth et al., 2014; Jeltsch-Thömmes & Joos, 2020). Spatial gradients within the ocean are important and influence, for example, the isotopic composition of the burial flux of organic and $CaCO_3$ particles into the lithosphere (Jeltsch-Thömmes & Joos, 2020). Earlier model studies on glacial-interglacial change considered the effect of sedimentary carbonate burial and dissolution on perturbations in atmospheric CO_2, but typically neglected organic matter burial (e.g., Broecker & Peng, 1987, 1989; Emerson & Archer, 1992; Archer & Maier-Reimer, 1994; Sigman et al., 1998; Archer et al., 2000; Sigman & Boyle, 2000; Sigman et al., 2010; Brovkin et al., 2012; Ganopolski & Brovkin, 2017; Willeit et al., 2019). Further studies show that feedbacks between organic matter burial, marine nutrient concentrations, and biological productivity are important (Tschumi et al., 2011; Menviel et al., 2012; Cartapanis et al., 2018; Jeltsch-Thömmes et al., 2019; Komar & Zeebe, 2021) and can strongly amplify perturbations in atmospheric CO_2 on glacial-interglacial time scales (Roth et al., 2014). Input-burial imbalances arising from changes in the burial fluxes of opal and carbonate or the weathering rates of silicate and carbonate rocks (e.g., Munhoven & François, 1996; Munhoven, 2002; Clark et al., 2006; Willeit et al., 2019; Börker et al., 2020; Köhler & Munhoven, 2020), or changes in CO_2 outgassing associated with volcanism (Huybers & Langmuir, 2009; Roth & Joos, 2012) have been invoked as possible contributing processes to explain glacial–interglacial variations and the Neogene cooling (23 to 2.6 million years ago) (e.g., Caves et al., 2016; Rugenstein et al., 2019). On even longer timescales, covering Earth's history, the coupled carbon-silica cycle is thought to stabilize climate on Earth via negative feedbacks in weathering of carbonate and silicate rocks (e.g., Walker et al., 1981; Berner, 1990; Ridgwell & Zeebe, 2005; Stolper et al., 2016; Kasting, 2019; Isson et al., 2020). Net organic matter accumulation in sediments and the accumulation of the oxidizing capacity at Earth's surface is reconstructed from $\delta^{13}C$ recorded in carbonate deposits (Broecker, 1970; Schrag et al., 2013; Mills et al., 2017). Models applied to quantitatively interpret the $\delta^{13}C$ carbonate records typically treat the fast exchanging reservoirs (atmosphere, ocean, ocean sediments, and land biosphere) as a single boxes to facilitate long simulations (Berner, 2006; Bergman et al., 2004).

Cost-efficient substitute models, which capture the spatial and temporal responses of more complex models, could be constructed and applied to study input-burial imbalances instead of box models. The substitute (or emulator) can be used to explore responses over long time scales or to run many sensitivity studies, which are computationally inaccessible with more comprehensive and therefore more expensive models. The spatio-temporal response of a complex model, its Green's function, can be captured in an idealized model simulation where the forcing is changed in a step- or pulse-like manner (e.g., Maier-Reimer & Hasselmann, 1987; Joos & Bruno, 1996; Thompson & Randerson, 1999; Hooss et al., 2001; Joos et al., 2013; Metzler et al., 2018; Strassmann & Joos, 2018; Bastiaansen et al., 2021). Idealized response simulations allow for a better understanding of underlying processes as they reveal the characteristic timescales and spatial patterns of the system's adjustment to an external perturbation, e.g., a change in weathering. While the processes and timescales affecting CO_2 have been investigated in several step-change experiments (e.g., Archer & Maier-Reimer, 1994; Sigman et al., 1998; Tschumi et al., 2011), to our knowledge no studies so far have systematically investigated the effect of changes in weathering input fluxes on both, carbon and carbon isotope budgets.

Here, we use the Bern3D Earth system model of intermediate complexity to perform idealized, up to 600 kyr long simulations. The weathering input fluxes of alkalinity, nutrients, carbon, and $\delta^{13}C$ are changed in a step-wise manner. The aim is to gen-

erate Green's functions and to understand the spatial and temporal responses in carbon inventories and $\delta^{13}C$ in the atmosphere and ocean, and changes in marine biogeochemical cycling as well as the evolution of input-burial imbalances. We quantify the contribution to the carbon and carbon isotopic perturbations from the organic carbon and $CaCO_3$ cycles and highlight the role of vertical gradients in $\delta^{13}C$ in the ocean. The response is used to build a cost-efficient substitute model to simulate the response in CO_2, CO_3^{2-}, and $\delta^{13}C_{DIC}$ to different weathering scenarios over the past 800 kyr.

2 Model Description and Experimental Set up

2.1 Model Description

The Bern3D v2.0s intermediate complexity model couples a single layer energy-moisture balance atmosphere with a thermodynamic sea-ice component (Ritz et al., 2011), a 3D geostrophic-frictional balance ocean (Edwards et al., 1998; Müller et al., 2006) with an isopycnal diffusion scheme and Gent-McWilliams parameterization for eddy-induced transport (Griffies, 1998), and a 10-layer ocean sediment module (Heinze et al., 1999; Tschumi et al., 2011; Jeltsch-Thömmes et al., 2019). The horizontal resolution across Bern3D model components is 41×40 grid cells and 32 logarithmically spaced depth layers in the ocean (Roth et al., 2014). Wind stress is prescribed from the NCEP/NCAR monthly wind stress climatology (Kalnay et al., 1996), and gas exchange at the ocean surface and calculation of carbonate chemistry follow OCMIP-2 protocols (Najjar & Orr, 1999; Wanninkhof, 2014; Orr & Epitalon, 2015), with an adjusted gas transfer dependency on wind speed (Müller et al., 2008). In the ocean, marine productivity is restricted to the euphotic zone (75 m) and calculated as a function of light availability, temperature, and nutrient concentrations (P, Fe, Si; Parekh et al., 2008; Tschumi et al., 2011).

The sediment module covers the top 10 cm and dynamically calculates the transport, redissolution/remineralization, and bioturbation of solid material, the pore water chemistry, and diffusion (see Tschumi et al., 2011). Burial (loss) of phosphorus, silica, carbon, and alkalinity from the sediment to the lithosphere is balanced by a variable input flux to the coastal surface ocean during spin-up. These weathering input fluxes are set equal to burial fluxes at the end of the spin-up for transient simulations. Iron is added to the model ocean by prescribed fluxes from aeolian deposition and continental margins and removed by particle scavenging (Parekh et al., 2008). Iron is not included in the sediment module.

The model is coupled to a 4-box representation of the land-biosphere carbon reservoirs (Siegenthaler & Oeschger, 1987). Here, the only purpose of this 4-box carbon reservoir model is to represent the dilution of atmospheric isotopic perturbations by the land biosphere, while other processes and changes in land carbon stocks are not considered.

Implementation of ^{13}C in the Model

^{13}C is implemented as a tracer in all Bern3D model components such that ^{13}C fluxes and inventories can be explicitly simulated across the atmosphere-ocean-land biosphere-reactive ocean sediments (AOBS) system. Fractionation of ^{13}C is considered for atmosphere-ocean gas transfer, carbonate chemistry, the formation of $CaCO_3$, POC and DOC, and during photosynthesis on land. Fractionation during photosynthesis on land is kept fixed; the simple 4-box model, applied here for computational reasons, does not represent changes in C3 and C4 plants nor changes in their discrimination. This is an uncertainty. No fractionation is considered for the remineralization of organic carbon in the ocean and on land. Formulations on how fractionation is calculated and corresponding references are summarized in table 1.

Table 1. Equations describing the fractionation in the model. T denotes sea surface temperature in Kelvin, and $[CO_{2,aq}]$ aqueous CO_2 in $\mu mol\,kg^{-1}$.
References: [a] Siegenthaler and Muennich (1981), [b] Mook (1986), [c] Freeman and Hayes (1992), [d] Siegenthaler and Oeschger (1987)

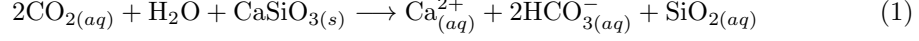| domain	formulation
air-sea[a,b]	$\alpha_{a\to s} = (1 - 0.0005 - 0.0002) \cdot \left(1 - \frac{0.373}{T} + 0.00019\right)$
carbonate chemistry[b]	$\alpha_{CO_{2,aq}\leftrightarrow HCO_3^-} = \left(1 - \frac{9.866}{T} + 0.02412\right)$
	$\alpha_{HCO_3^- \leftrightarrow CO_3^{2-}} = \left(1 - \frac{0.867}{T} + 0.00252\right)$
	$\alpha_{CO_{2,aq}\leftrightarrow DIC} = \dfrac{DIC}{[CO_{2,aq}] + \frac{\left[HCO_3^-\right]}{\alpha_{CO_{2,aq}\leftrightarrow HCO_3^-}} + \frac{\left[CO_3^{2-}\right]\cdot\alpha_{HCO_3^-\leftrightarrow CO_3^{2-}}}{\alpha_{CO_{2,aq}\leftrightarrow HCO_3^-}}}$
sea-air[b]	$\alpha_{s\to a} = (1 - 0.0005 - 0.0002) \cdot \alpha_{CO_{2,aq}\leftrightarrow DIC}$
$CaCO_3$ formation[b]	$\alpha_{HCO_3^-\to CaCO_3} = \left(1 - \frac{4.232}{T} + 0.0151\right)$
marine photosynthesis[c]	$\alpha_{[CO_2]\to C_{org}} = (1.00119 + 0.01203 \cdot \log_{10}([CO_{2,aq}]))$
terrestrial photosynthesis[d]	constant fractionation of -18.1 ‰

Implementation of Weathering Input Fluxes in the Model

The loss of carbon (C), silica (Si), alkalinity (ALK), and phosphorus (P) from the open ocean through sedimentary burial is counteracted by the input of weathered material to the open ocean. In the model, this is implemented in an idealized way: the loss fluxes of tracers through burial of material in the lithosphere are, in steady state, balanced by input fluxes of equal size. The elemental ratios (^{12}C:^{13}C:Si:ALK:P) of the input flux to the open ocean are therefore dictated by the elemental ratios of the global burial flux at the end of the spin up. Throughout the manuscript, these fluxes to the ocean will be referred to as input fluxes.

C, Si, P, and ALK input are uniformly added to the corresponding dissolved inorganic tracer concentrations of the near-coastal surface grid cells in Bern3D. Thus, we do not represent reprocessing of elements, e.g., by the land biosphere or in estuaries, nor different forms of input such as dissolved and particulate organic matter, or P attached to surfaces of iron-manganese and hydroxide particles (Compton et al., 2000; Lacroix et al., 2021). Atmospheric deposition of C, Si, ALK, and P may be viewed as included in the input fluxes. This simplification appears justified as the different forms of input eventually enter the inorganic pools on time scales shorter than the multi-millennial timescales
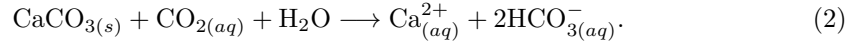
addressed in this study. We attribute the elemental input fluxes conceptually to different processes such as silicate and carbonate weathering.

Input from 1 mol $CaSiO_3$ adds one mole of Si, two moles of alkalinity, and no carbon to the model ocean. This is a short-circuit of the atmosphere following the simplified reaction for weathering of tectosilicates (e.g., Colbourn et al., 2013):

$$2CO_{2(aq)} + H_2O + CaSiO_{3(s)} \longrightarrow Ca^{2+}_{(aq)} + 2HCO^-_{3(aq)} + SiO_{2(aq)} \tag{1}$$

Two moles of carbon are removed from the atmosphere-ocean system in the form of CO_2 and two moles of alkalinity and carbon in the form of HCO^-_3 are added to the ocean. On the timescales considered here, the atmosphere and surface ocean can be considered well mixed and we do not represent the outgassing of CO_2 and the related interhemispheric ocean carbon transport arising from the riverine carbon inputs (Sarmiento et al., 1992; Lacroix et al., 2020).

Weathering of carbonate rocks ($CaCO_3$) is given by (e.g., Goodwin & Ridgwell, 2010):

$$CaCO_{3(s)} + CO_{2(aq)} + H_2O \longrightarrow Ca^{2+}_{(aq)} + 2HCO^-_{3(aq)}. \tag{2}$$

In the model, two moles of alkalinity for each mole of carbon are added. This is again a short-circuit of the atmosphere.

Input fluxes (F) of P, Si, ALK, DIC, and ^{13}C(DIC) are attributed to the weathering flux from carbonate rocks, F_{CaCO_3}, silicate rocks, F_{CaSiO_3}, an assumed conceptual input flux releasing the elements of former organic material, F_{org} (from hereon referred to as organic input flux), and a remainder flux, $F_{remainder}$, to close the carbon and carbon isotopic budget of the model in equilibrium. $F_{remainder}$ is thought of as CO_2 emissions from volcanism and tectonic outgassing. The input F_{org} should not be confused with a flux of organic material as all input fluxes are added to the inorganic tracer pools in Bern3D. At steady state, the global elemental fluxes of F_{org} are equal to those of the global burial flux of particulate organic matter. The fluxes are related to each other in molar units:

$$F_P = \mathcal{R}_{P:C} \cdot F_{org} \tag{3}$$

$$F_{Si} = F_{CaSiO_3} \tag{4}$$

$$F_{ALK} = 2 \cdot F_{CaSiO_3} + 2 \cdot F_{CaCO_3} + \mathcal{R}_{ALK:P} \cdot \mathcal{R}_{P:C} \cdot F_{org} \tag{5}$$

$$F_{DIC} = F_{CaCO_3} + F_{org} + F_{remainder} \tag{6}$$

$$F_{DIC-13} = F_{CaCO_3} \cdot {}^{13}R_{CaCO_3} + F_{org} \cdot {}^{13}R_{org} + F_{remainder} \cdot {}^{13}R_{remainder} \tag{7}$$

$\mathcal{R}_{P:C}$ and $\mathcal{R}_{ALK:P}$ are the Redfield ratios of P:C = 1:117 and ALK:P = -17:1, respectively (L. A. Anderson & Sarmiento, 1994; Paulmier et al., 2009). ^{13}R denotes the $^{13}C/C$ isotopic ratio.

The burial fluxes of P, Si, ALK, DIC, and ^{13}C(DIC) are diagnosed at the end of the model spin-up and prescribed as the input fluxes for these components (F_P, F_{Si}, F_{ALK}, F_{DIC}, F_{DIC-13}) at the start of transient simulations. $^{13}R_{CaCO_3}$ and $^{13}R_{org}$ are diagnosed from the signatures of the $CaCO_3$ and particulate organic carbon (POC) burial. $^{13}R_{remainder}$ is the signature needed to close the ^{13}C budget of the model in equilibrium after the spin-up. We assume no fractionation for $CaSiO_3$ weathering. All input is assumed to be free of ^{14}C. Eq. 3 to 7 are solved for the steady-state fluxes (F_{org}, F_{CaSiO_3}, F_{CaCO_3}, $F_{remainder}$), and the signature $^{13}R_{remainder}$. Table 2 shows steady state fluxes and inventories of $CaCO_3$, POC, and opal, as well as $\delta^{13}C$ signatures. $\delta^{13}C$ of the export flux is not diagnosed in the current model setup.

Table 2. Export, deposition, and burial fluxes as well as sediment inventories of $CaCO_3$, opal, and particulate organic carbon (POC) and $\delta^{13}C$ signatures, determined as the mean of the first 100 years after a pre-industrial spin-up in the control run, and corresponding literature estimates. References: [a] Battaglia et al. (2016), [b] Tréguer et al. (2021), [c] Sarmiento and Gruber (2006), [d] Milliman and Droxler (1996), [e] Feely et al. (2004)

variable	units	Bern3D	observational estimates	$\delta^{13}C$ in ‰
Export				
$CaCO_3$	GtC yr^{-1}	0.98	0.72-1.05[a]	
opal	Tmol Si yr^{-1}	110.02	112[b]	
POC	GtC yr^{-1}	11.93	6.5-13.1[c]	
Deposition				
$CaCO_3$	GtC yr^{-1}	0.49	0.5[d]	2.91
opal	Tmol Si yr^{-1}	77.6	84[b]	
POC	GtC yr^{-1}	0.65	1.7-3.3[c]	-20.39
Burial				
$CaCO_3$	GtC yr^{-1}	0.22	0.1-0.14[e]	2.88
opal/F_{Si}	Tmol Si yr^{-1}	6.72	9.2[b]	
POC/F_{org}	GtC yr^{-1}	0.24	0.12-0.26[c]	-20.42
F_{ALK}	Gt eq. yr^{-1}	0.41		
F_{DIC}	GtC yr^{-1}	0.46		-9.09
Reactive ocean sediments				
$CaCO_3$	GtC	939		3.05
opal	Tmol Si	20,658		
POC	GtC	516		-20.13
Input				
F_{CaCO_3}	GtC yr^{-1}	0.14		2.88
F_{CaSiO_3}	Tmol Si yr^{-1}	6.72		
F_{org}	GtC yr^{-1}	0.24		-20.42
$F_{remainder}$	GtC yr^{-1}	0.08		2.88

2.2 Experimental Set-up and Analysis

The model is spun up over 60 thousand years (kyr) under 1765 CE boundary conditions. An atmospheric CO_2 concentration of 277.8 ppm with an isotopic signature of $\delta^{13}C_{atm}$ = -6.305 ‰ and $\Delta^{14}C_{atm}$ = 0 ‰ is prescribed. From the 1765 CE steady state, at nominal year -100, 100.1 kyr long experiments are started. After 100 years, i.e., in nominal year 0 of the experiments, step-changes in F_{CaCO_3} and F_{org} from -80% to +80% in steps of 20% are applied. The corresponding amounts of carbon, ^{13}C, alkalinity, and P (Eqs. 3-7) are then added to the coastal surface ocean. A subset of the above experiments, namely the changes of +40%, -40%, and the control run, are extended by an additional 500 kyr simulation period in order for the model to establish new equilibrium after the step-change in carbon isotopes.

For organic input, an additional 100 kyr sensitivity experiment is performed to investigate the effect of differences in the $\mathcal{R}_{P:C}$ ratio. To this mean, 30% of the P entering marine sediments is immediately dissolved back into the ocean. This P leaching changes the sedimentary and therefore also the input flux $\mathcal{R}_{P:C}$ to about 1 : 152. Our setup for changing F_{org} is different from a step-change in the ocean P inventory as applied by Tschumi

et al. (2011) and others. In the experiments presented in this study, the change in F_{org} implies a sustained change in the input fluxes of P, C, ^{13}C, and ALK.

Results presented in this study are relative to a control run to account for any drift over the 600 thousand year (kyr) simulation period. Generally, drift is small, and amounts, for example in the case of CO_2, to well below 0.01 ppm kyr^{-1} in the control simulation. The output frequency for marine 3-D tracer fields after the perturbation is every 10 years during the first 1 kyr, every 200 years until 10 kyr, every 1 kyr until 100 kyr, and every 5 kyr thereafter.

Changes in the carbon isotopic fluxes and inventories are expressed in [GtC ‰] by multiplying inventories or fluxes of carbon [GtC] with their corresponding δ^{13}C signatures [‰]. We attribute the change in the isotopic burial minus input flux to changes (Δ) in carbon burial (B) and input (I) fluxes and in the isotopic signature of the burial flux (δ_B) relative to the equilibrium state after the spin-up (subscript 0) for both POC and $CaCO_3$:

$$
\begin{aligned}
^{13}B - {}^{13}I &= (B_0 + \Delta B) \cdot (\delta_0 + \Delta \delta_B) - (I_0 + \Delta I) \cdot \delta_0 \\
&= \Delta(B - I) \cdot \delta_0 + B_0 \cdot \Delta \delta_B + \Delta B \cdot \Delta \delta_B
\end{aligned}
\tag{8}
$$

Note that the steady state carbon and isotopic burial-input fluxes vanish with $B_0 - I_0 = 0$ and $\delta_{B,0} = \delta_{I,0} = \delta_0$.

2.3 Green's Function Substitute Model

Green's functions for a change in input flux (weathering) are directly obtained from the step-change simulations with Bern3D. Generally, the Green's function can be determined by prescribing a step-like change in forcing (e.g., the magnitude of weathering flux) in a model previously spun up to equilibrium. Then the model is run towards a new equilibrium and the simulated change $\Delta y(\vec{x}, \tau)$ of any variable of interest (e.g., $\delta^{13}C_{\text{DIC}}$) is monitored. The response Δy is normalized by the magnitude of the step change to yield the Green's function, $r^y(\vec{x}, \tau)$. τ is the time passed since the step-like change and $\vec{x}$ indicates location.

Any forcing history, $F(t)$, may be approximated by a series of small step-like changes, $\Delta F(t_i)$. Then, the response, $\Delta y(\vec{x}, t)$, in variable y at time t and location $\vec{x}$ to this forcing history is for a linear system:

$$
\Delta y(\vec{x}, t) = \sum_i \Delta F(t_i) \cdot r^y(\vec{x}, t - t_i).
\tag{9}
$$

$t - t_i$ represents the time τ_i that has passed since the step change $\Delta F(t_i)$ at time t_i. The sum is over all step changes used to approximate the forcing history from its beginning up to time t. The system is assumed in equilibrium at the start of the forcing time series.

Instead of running a complex 3-dimensional dynamic model, its response is approximated by Eq. 9, a great efficiency gain. For further ease of application, a Green's function can be approximated using Principal Component-Empirical Orthogonal Functions (PC-EOF). The temporal component of the PC-EOF can be approximated by a sum of exponential terms and the substitute model (Eq. 9) can be represented by a series of box models and spatial patterns for further computational efficiency. (see Joos et al., 2001; Strassmann & Joos, 2018; Jeltsch-Thömmes & Joos, 2020).

The dynamics of a linear system are fully characterized by its Green's function. Although the carbon cycle and the Earth system are not linear, the linear approximation of Eq. 9 is often useful. Here, we determined Greens's function over a wide range of step changes (-80% to +80% of the unperturbed flux) to evaluate non-linearities. In the dis-

328 cussion in section 4.2, we will apply Eq. 9 for different weathering scenarios, using di-
329 rectly the (normalized) model output from the step simulations described in section 2.2.

3 Results

3.1 Earth System Response to a 40% Increase in the CaCO$_3$ Weathering Input Flux

333 We first address Earth system responses to changes in CaCO$_3$ weathering. The pre-
334 scribed 40% step-like increase in the CaCO$_3$ weathering flux translates into an increase
335 in the inputs of carbon and alkalinity in a 1:2 molar ratio (Fig. 1a-b). The δ^{13}C signa-
336 ture of the total carbon input is also increased by 1.3‰ (Fig. 1c) because the relative
337 share of the isotopically heavy CaCO$_3$ weathering input becomes larger. The individ-
338 ual δ^{13}C signatures of the CaCO$_3$ and POC input remain unchanged in our setup.

339 In response to the step-increase in carbon and alkalinity (ALK) input, a new equi-
340 librium of the climate-carbon system is approached with an e-folding timescale (τ) of
341 about 10 thousand years (kyr, Fig. 1d-l; 2a). In other words, concentrations and fluxes
342 typically change most rapidly immediately after the step and then slowly approach a new
343 equilibrium following roughly an exponential curve. As a remarkable exception, δ^{13}C iso-
344 topic signatures continue to change over a few 100 thousand years (Fig. 1m). Possible
345 fits of the responses in ΔCO$_2$ and $\Delta\delta^{13}$C$_{\text{DIC}}$ are provided as equations in Fig. 1.

346 Atmospheric CO$_2$ decreases, by almost 32 ppm (Fig. 1d), as the surface ocean con-
347 centration of ALK increases about twice as much as that of dissolved inorganic carbon
348 (DIC) (Fig. 1f,g). Surface air temperature (SAT) decreases by about 0.5 °C (Fig. 1e)
349 in response to lower atmospheric CO$_2$. DIC and ALK increase by about 37 and 68 mmol
350 m^{-3} on ocean average (Fig. 1f,g). Due to this "ocean alkalinization", ocean pH, and car-
351 bonate ion concentration increase in the surface and deep ocean, and the calcium car-
352 bonate saturation horizon deepens on average by about 700 m in the North Pacific (Fig.
353 1h-j). In turn, marine biogenic CaCO$_3$ is better preserved in ocean sediments, and the
354 net transfer of CaCO$_3$ from the ocean to the sediments, and eventually the lithosphere,
355 increases by about 25% (Fig. 1l). The equilibrium increase in CaCO$_3$ burial of 25% cor-
356 responds to the implied increase in the Ca^{2+} input of 25% in our scenario which results
357 from constant F_{CaSiO_3} and a 40% increase in F_{CaCO_3}. The modeled saturation horizon
358 in the equatorial Atlantic was already relatively close to the ocean bottom before the step-
359 change in input, leaving little room for further deepening (Fig. 1i). The timescale of this
360 carbonate compensation process ($\sim$8-10 kyr, e.g. Archer et al., 1997, 1998; Jeltsch-Thömmes
361 & Joos, 2020) is reflected in the timescale of the CO$_2$ perturbation of $\sim$10 kyr.

362 Changes in global export fluxes of particulate organic matter (POM), CaCO$_3$, and
363 opal are comparably small ($<$3%, Fig. 1k) and result in only small declines in the sed-
364 imentary POM and opal inventories (Fig. 1l). Export production generally decreases as
365 a result of lower temperatures and increased sea-ice area, with the largest changes in the
366 Southern Ocean. The higher input of ALK to the surface ocean (Fig 1a), together with
367 the slight reduction in CaCO$_3$ export (Fig 1k), causes a larger increase of ALK in the
368 surface than the deep ocean (Fig 1g), while the surface-to-deep gradient in DIC remains
369 almost unaffected by the increase in CaCO$_3$ weathering (Fig 1f).

370 We establish budgets for the carbon (Fig. 2a) and alkalinity perturbations by com-
371 paring accumulated burial-input imbalances for CaCO$_3$ and POM with changes in the
372 major reservoirs, atmosphere, ocean, and sediments. Carbon and ALK fluxes are sto-
373 ichiometrically linked. C:ALK molar ratios of 1:2 and 117:-17 are applied for CaCO$_3$ and
374 POM and the molar weight of carbon is 12.01 g mol^{-1}. Carbon and alkalinity storage
375 in the ocean increases by about 600 GtC and 91 Petamol eq, respectively. The major-
376 ity of the perturbation in the combined atmosphere-ocean system ($\sim$521 GtC; 91 Pmol
377 eq) and the reactive ocean sediments ($\sim$334 GtC; 60 Petamol eq) is driven by imbalances
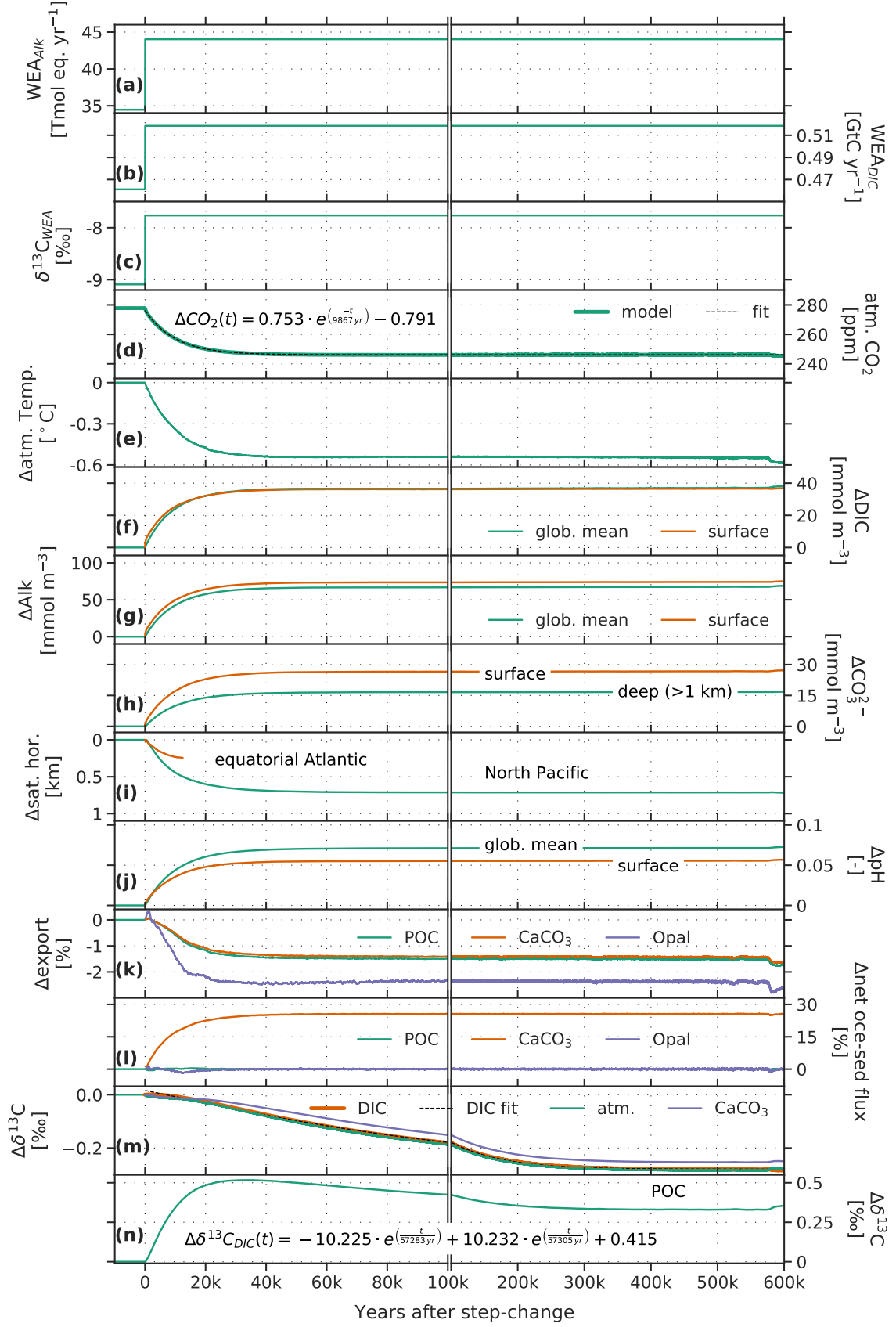
Figure 1. Timeseries evolution of the forcing (a-c) and a set of Earth system properties (d-n) for a 40% step increase in the CaCO₃ input flux. For better visibility, data in panels e, k, l, and m (only CaCO₃) is shown as 100 yr running means. Surface refers to upper 100 m.
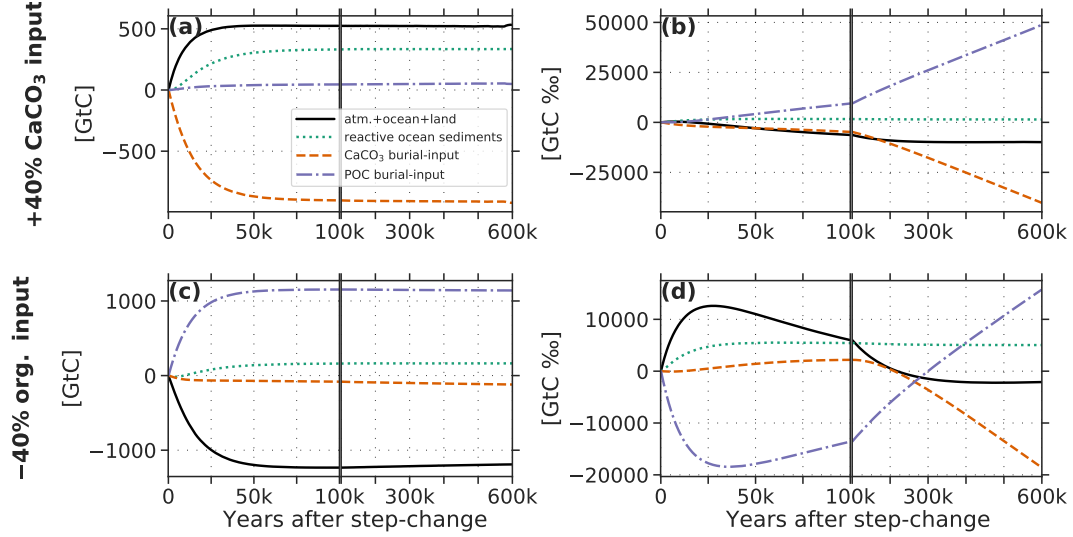
Figure 2. Carbon (a,c) and carbon isotopic (b,d) budget for step-changes of +40% and -40% in the CaCO$_3$ (a,b) and organic (c,d) input flux.

in the CaCO$_3$ burial-input flux ($\sim$-912 GtC; 152 Petamol eq). Contributions from imbalances associated with the POM cycle are small ($\sim$53 GtC; -0.6 Petamol eq) (Fig. 2a). Accordingly, the majority of change in the reactive ocean sediments is explained by an increased CaCO$_3$ content ($\sim$361 GtC; 60 Petamol eq) with little contribution from decreased POM storage ($\sim$-27 GtC; 0.3 Petamol eq). The values refer to means over the period 500-550 kyr after the step change.

Carbon Isotopes

After an initial small increase, resulting from the higher δ^{13}C signature of the weathering input after the step-change (Fig. 1c), δ^{13}C decreases gradually after the step in the atmosphere, ocean, land biosphere (AOB), and sedimentary CaCO$_3$ reservoirs. δ^{13}C in these reservoirs stabilizes at about -0.28 ‰ lower values after several hundred kyr (Fig. 1n). In contrast, δ^{13}C of sedimentary POC increases relatively fast to peak at around 30 kyr after the step. Afterwards, the anomaly decreases slightly to stabilize at about 0.35 ‰ after several hundred kyr (Fig. 1m).

The δ^{13}C perturbation budget is shown in (Fig. 2b). The accumulated isotopic perturbation in the AOB system stabilizes at $\sim$-9800 GtC ‰ after several hundred kyr (Fig. 2b, black line). The change is mainly linked to the decrease in the mean isotopic signature of the constituents of the AOB system (Fig. 1m); The contribution from the change in the carbon inventory of the AOB system is small (not shown). The perturbation in reactive sediments accumulates to $\sim$+1500 GtC ‰(Fig. 2b, green dotted). This positive perturbation is mainly due to the decrease in the sedimentary POC inventory, with further contributions from the change in POC signature and from CaCO$_3$.

The equilibration of δ^{13}C after the change in CaCO$_3$ input is controlled by burial-input imbalances in both the CaCO$_3$ and POC cycles (Fig. 2b). This is different than for carbon for which burial-input imbalances of CaCO$_3$ dominate the response (Fig. 2a). The δ^{13}C perturbation in the AOBS system is stabilized by the canceling effects of POC versus CaCO$_3$ burial-input flux. While the POC burial-input flux removes ^{13}C from the system, the CaCO$_3$ burial-input flux adds ^{13}C (Fig. 2b, magenta versus orange lines).

For further understanding, we attribute the net isotopic fluxes of POC and CaCO$_3$ burial-input according to Eq. 8 (Fig. 3a-c). The three terms considered are linked to changes

408 in the net burial-input carbon flux ($\Delta(B-I)\cdot\delta_0$), in the $\delta^{13}C$ signature of the burial
409 flux ($\Delta\delta_B \cdot B_0$), and the perturbations in the burial carbon flux and signature ($\Delta B \cdot$
410 $\Delta\delta_B$) (Fig. 3). The majority of the carbon isotopic perturbation in response to a 40%
411 increase in $CaCO_3$ input is caused through changes in the $\delta^{13}C$ signatures of the POC
412 and $CaCO_3$ burial fluxes (Fig. 3b). Lower atmospheric CO_2 (Fig. 1d) and therefore lower
413 surface water $[CO_{2,aq}]$ reduces fractionation during marine photosynthesis (see Table 1).
414 As a result, $\delta^{13}C$ of the POC export flux increases, and the mean $\delta^{13}C$ of sedimentary
415 POC peaks about 30 kyr after the step change in $CaCO_3$ input (Fig. 1n). Consequently,
416 $\delta^{13}C$ of the POC burial flux increases, and ^{13}C is removed by POC burial-input. This
417 removal causes $\delta^{13}C$ of DIC to decrease (Fig. 1m; 2b). The negative perturbation in $\delta^{13}C_{DIC}$
418 is incorporated into newly formed $CaCO_3$ and POC, explaining the gradual decrease in
419 $\delta^{13}C$ of the $CaCO_3$ sediment inventory (Fig. 1m) and burial flux, and the post-peak de-
420 crease in the $\delta^{13}C$ signature of the POC sediment inventory (Fig. 1n).

421 Changes in the carbon isotopic budget due to the carbon burial-input imbalance
422 ($\Delta(B-I)\,\delta_0$) are comparably small (Fig. 3a). They are larger for $CaCO_3$ than for POC
423 as a result of the larger cumulative change in the burial-input flux for $CaCO_3$ than for
424 POC (Fig. 2a). For the same reason, the contribution of $\Delta B \cdot \Delta\delta$ is substantially larger
425 for $CaCO_3$ ($\sim$ 8000 GtC‰) than POC ($\sim$ 0 GtC‰) (Fig. 3c).

426 The perturbation in $\delta^{13}C_{DIC}$ varies spatially within the ocean. The surface-to-thermocline
427 gradient in $\delta^{13}C_{DIC}$ is reduced after the step in $CaCO_3$ input. In Fig. 5a horizontally-
428 averaged $\Delta\delta^{13}C_{DIC}$ is plotted versus time and depth. $\Delta\delta^{13}C_{DIC}$ is on average slightly
429 less negative in the thermocline than in surface and deep ocean waters. The differences
430 of $\Delta\delta^{13}C_{DIC}$ in surface versus $\Delta\delta^{13}C_{DIC}$ of thermocline and deep waters are small, <0.05
431 ‰ on average (Fig. 5c). They are a consequence of reduced fractionation during ma-
432 rine photosynthesis resulting from lower $[CO_{2,aq}]$. Thus, the POC flux transports a less
433 negative isotopic signal from the surface to the thermocline, where most of the POC is
434 remineralized. Changes in circulation could contribute to a different $\delta^{13}C_{DIC}$ gradient
435 but variations in modeled ideal age of water masses are very small (<10 years, not shown).
436 The response to a 40% decrease in $CaCO_3$ input yields a very similar response but with
437 inverse sign (Fig. 5b,c) and is not further discussed here.

438 In summary, the carbon-climate system equilibrates typically within a few tens of
439 kyr after the step change in $CaCO_3$ input, whereas it takes several hundred kyr to es-
440 tablish a new equilibrium for $\delta^{13}C$ signatures. Changes in proxy-related variables are a
441 decrease in CO_2 and SAT, an increase in carbonate ion concentration with deepening
442 of the lysocline and higher carbonate preservation, near absent or small responses in POM
443 and opal bulk fluxes, and a long-term decrease in $\delta^{13}C$ of atmospheric CO_2 and DIC with
444 a slightly reduced surface-to-thermocline gradient in $\delta^{13}C_{DIC}$.

445 Remarkably, changes in $CaCO_3$ input cause changes in $\delta^{13}C$ of DIC and atmospheric
446 CO_2 of several tenths of a permil. Such $\delta^{13}C$ changes are comparable to reconstructed
447 changes over glacial-interglacial cycles. Also remarkable, the change in $\delta^{13}C$ of $CaCO_3$
448 and DIC is with -0.2‰ opposite to the change in the signature of the input flux of +1.3‰.
449 This is different to expectations of equal change in $\delta^{13}C$ signatures when treating the
450 climate system as one box (e.g., Eq. 1 in (Schrag et al., 2013)) and neglecting changes
451 in fractionation. The contribution of the POM cycle, in particular a smaller isotopic frac-
452 tionation during marine photosynthesis under lower CO_2, is key to understanding the
453 isotopic changes. These $\delta^{13}C$ changes become only evident when considering the reor-
454 ganization of the carbon cycle within the climate system instead of treating the climate
455 system as a single reservoir and when considering POC input and burial fluxes in ad-
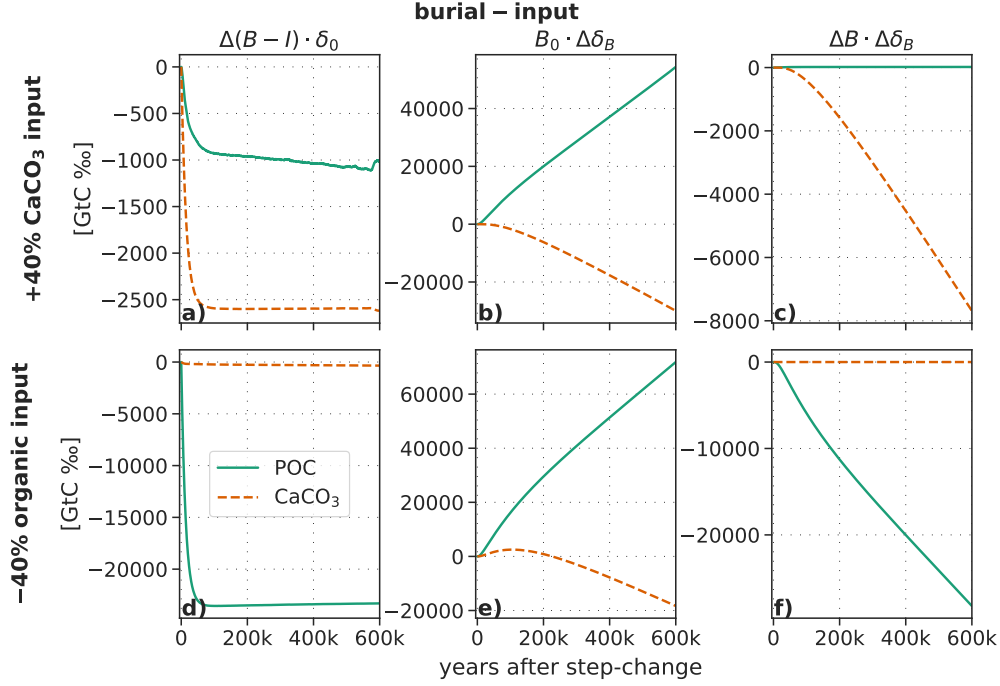456 dition to $CaCO_3$ input-burial imbalances.

Figure 3. Cumulative contribution of the burial-input flux to the carbon isotopic perturbation for a (a,b,c) 40% increase in the CaCO$_3$ and a (d,e,f) 40% decrease in the organic input flux. The contribution is split into changes in the (a,d) carbon flux ($\delta_0 \cdot \Delta F$), the (b,e) δ^{13}C signature ($\Delta\delta \cdot F_0$) of the flux, and their (c,f) combination ($\Delta\delta \cdot \Delta F$).

3.2 Earth System Response to a 40% Decrease in the Organic Input Flux

A 40% decrease in the organic input flux reduces P and carbon inputs, increases the alkalinity input, and leads to an enrichment in the δ^{13}C signature of the total carbon input (Fig. 4a-d). Similar as for the change in CaCO$_3$ input, most carbon cycle fluxes and tracers adjust after the step-change towards a new equilibrium on time scales of order ~7.5 kyr (Fig. 4e-m). Exceptions are the CaCO$_3$ ocean-to-sediment flux which is only temporarily perturbed (Fig. 4m, orange lines), and δ^{13}C signatures which show changes over several hundred kyr (Fig. 4n,o). The e-folding timescale for the fit of the atmospheric CO$_2$ perturbation is different from the CaCO$_3$ step-change experiment, as the underlying processes differ. While in the case of the CaCO$_3$ step-change experiment, CaCO$_3$ compensation is the controlling process, in the case of the organic step-change, an interplay between changes in POC export production and burial rates, mediated by changes in the phosphorous inventory are at play, as described in detail below.

In response to the step-reduction in carbon input, DIC, atmospheric CO$_2$, and temperature decrease (Fig. 4e-g). In the steady state solution of the model, the organic input flux contributes about half of the carbon input (Table 2). Modeled changes in the atmospheric and marine carbon inventory are thus a direct result of reduced carbon input after the step-change.

The marine P inventory decreases as a result of the reduced P input, limiting biological productivity. Production and export of organic material, as well as of CaCO$_3$, decreases by about 23% (Fig. 4l). In turn, the POC flux to sediments and eventually POC burial decreases by 40%, thereby exactly offsetting the reduction in organic matter input at the new equilibrium. Opal export is only reduced by a couple of percents. At the
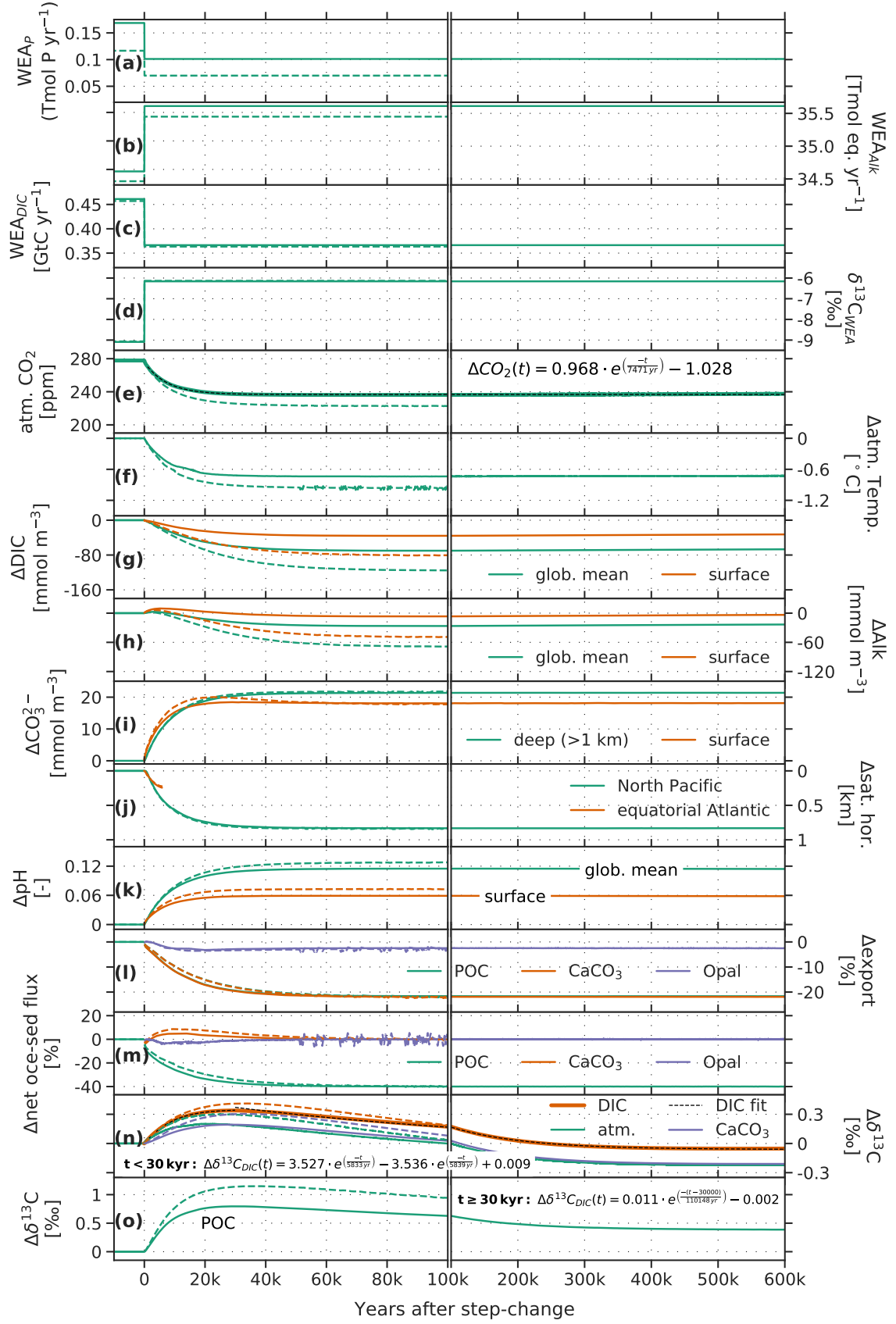
Figure 4. Timeseries evolution of the forcing (a-d) and a set of Earth system properties (e-o) for a 40% decrease in the organic input flux. Dashed colored lines show results from the sensitivity experiment with a sedimentary C:P ratio of ~152:1. For better visibility, data in panels f, l, m, and n (only CaCO₃) is shown as 100 yr running means. Surface refers to upper 100 m.

end of the simulation, opal export is reduced in high latitudes as a result of increased sea-ice cover, and increased in low- and mid-latitudes (not shown).

In response to reduced DIC, the carbonate ion concentration increases as $[CO_3^{2-}]$ $\sim$ [ALK]-[DIC]) (Fig. 4g-i). ALK input and ALK in the ocean changes only little during the first 10 kyr (Fig. 4b,h). The shift to a higher $[CO_3^{2-}]/[DIC]$ ratio goes hand in hand with an increase in pH (Fig. 4k). The increase in $[CO_3^{2-}]$ causes a deepening of the saturation horizon by about 800 m in the North Pacific (in the equatorial Atlantic the saturation was already relatively close to the ocean bottom before the step-change in input, leaving little room for further deepening Fig. 4j). In turn, more $CaCO_3$ is transferred from the ocean to the sediments in the first 50 kyr after the step change (Fig. 4m), despite the $\sim$23% reduction in $CaCO_3$ export. This $CaCO_3$ transfer lowers the ocean's ALK inventory (Fig. 4h), and the temporary perturbation in the $CaCO_3$ flux to sediments vanishes again (Fig. 4m).

These marine carbon cycle changes affect the surface-to-deep ocean gradients in DIC and ALK (Fig. 4g,h; red versus green lines). The decrease in DIC and ALK is larger in the deep ocean than in the surface, and the surface-to-deep gradient in DIC is reduced on global average. These changes in gradients are linked to the reduction in POC and $CaCO_3$ export, that tend to remove less carbon and slightly less alkalinity from the surface ocean.

Altogether, the AOB reservoir looses $\sim$1196 GtC (Fig. 2c). This change is driven by a cumulative burial-input imbalance in the POC cycle of $\sim$1142 GtC with little contribution from the $CaCO_3$ cycle ($\sim$-115 GtC) (Fig. 2c). The overall increase in carbon storage in reactive ocean sediments (163 GtC) is explained by a gain of $CaCO_3$ ($\sim$367 GtC) which is partly balanced by a loss of POC ($\sim$-203 GtC). Again, values refer to means over the period 500-550 kyr after the step change.

Carbon Isotopes

Less input of isotopically light organic carbon shifts the $\delta^{13}C$ signature of the atmosphere and ocean to higher values at first. Similarly, the $\delta^{13}C$ signature of the net ocean-sediment flux of carbon increases. After peaking at around 20 kyr, $\delta^{13}C$ in the atmosphere and ocean, as well as $\delta^{13}C$ of sedimentary POC and $CaCO_3$ (and therefore also the burial flux) decrease slowly to reach new steady-state values after several 100 kyr (Fig. 4n,o).

The driving processes of these changes take place on roughly two timescales (Fig. 2d; 3d-f). The timescales are caused by the different response times in the carbon ($\Delta(I-B)$) and carbon isotopic budgets. The carbon cycle approaches a new equilibrium after multiple millennia and can be seen as constant after roughly 50 kyr (Fig. 2c). The positive cumulative imbalance in the isotopically light POC burial-input (Fig. 2c, dashed purple line) leads to a reduced removal of ^{13}C from the reactive carbon pools (Fig. 2d, dashed purple line). This causes the initial increase in $\delta^{13}C$ in these reservoirs (Fig. 4n,o; 2d; 3d). This initial, shorter timescale, is reflected in the fit of the $\delta^{13}C_{DIC}$ perturbation for the first 30 kyr after the step-change (equation in panel n, Fig. 4).

In contrast, lower atmospheric CO_2 and therefore lower $[CO_{2,aq}]$ lead to less fractionation during marine photosynthesis and an increase in $\delta^{13}C$ of sedimentary POC (Fig. 4o) and the POC burial flux. Hereby, isotopically heavy carbon ^{13}C is continuously removed from the combined AOB carbon pool (Fig. 3e; 2d). On timescales of multiple 10 kyrs, the change in signature outweighs the effect of the increased cumulative burial-input flux on the carbon isotopic budget and the direction of change in $\delta^{13}C$ signatures is reverted (Fig. 4n,o; 2d). The longer timescale of this second phase of the $\delta^{13}C_{DIC}$ perturbation is reflected in the fit for $t > 30$ kyr (panel o, Fig. 4).

$\delta^{13}C$ of $CaCO_3$ follows surface ocean $\delta^{13}C_{DIC}$. The associated isotopic flux (Figs. 2d; 3e, dashed orange lines) eventually balances the effect of the POC cycle ((Figs. 2d;
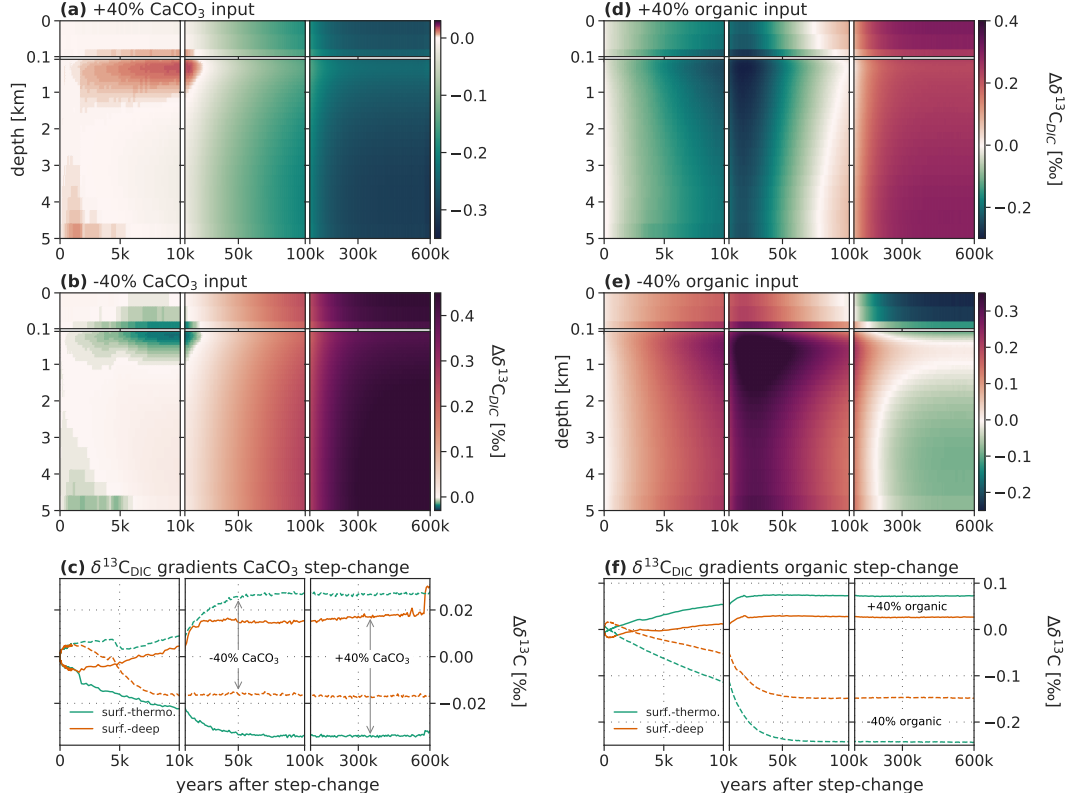
Figure 5. Hovmoeller-type diagram of the $\delta^{13}C_{DIC}$ perturbation for step-changes of (a,d) +40% in the CaCO₃ and organic input fluxes, (b,e) -40% in the CaCO₃ and organic input fluxes, and (c,f) timeseries of the surface (euphotic zone)-to-thermocline (∼600-700 m) and surface-to-deep (2.5-3.5 km) gradient for the respective experiments.

530 3d-f), green lines) on the carbon isotopic budget, leading to stable $\delta^{13}C$ in the AOB sys-
531 tem after 300 kyr (Fig. 4n; 2d).

532   The perturbation in the POC export causes a strong perturbation in the surface-
533 to-deep gradient of $\delta^{13}C_{DIC}$. Fig. 5e shows the horizontally-averaged evolution of the
534 perturbation in $\delta^{13}C_{DIC}$ after the step-like decrease in input of organic material. Both,
535 the reduction in the export of POC by about 23% (Fig. 4m, green line) and the increase
536 of its $\delta^{13}C$ signature (Fig. 4o) weaken the overall surface-to-thermocline and the surface-
537 to-deep gradient in $\delta^{13}C_{DIC}$. Changes in the export of labile dissolved organic matter
538 may also somewhat contribute. Further, changes in input minus burial fluxes also affect
539 spatial isotopic gradients. A clear perturbation in the gradient between the euphotic zone
540 (uppermost two vertical layers in the model) and the underlying waters develops, lead-
541 ing to strongly enriched $\delta^{13}C_{DIC}$ perturbation in thermocline and intermediate depth
542 waters, even reaching down to the ocean floor, as compared to the surface (see dark red
543 blob in Fig. 5e). After about 200 kyr a vertical perturbation pattern with a negative $\delta^{13}C_{DIC}$
544 perturbation in the surface, a slightly positive $\delta^{13}C_{DIC}$ perturbation in the thermocline
545 and intermediate depth waters, and a slightly negative $\delta^{13}C_{DIC}$ perturbation in waters
546 below ~2 km depth has developed and appears to prevail. The surface-to-thermocline
547 gradient is changed by ~0.25 ‰ and the surface-to-deep gradient by ~0.15 ‰ on global
548 average.

549   In the case of a 40% increase in organic material input, the spatio-temporal evo-
550 lution of $\Delta\delta^{13}C_{DIC}$ is generally comparable, however the absolute perturbation in global
551 mean $\delta^{13}C_{DIC}$ is initially smaller and stabilizes at higher levels, and changes in the surface-
552 thermocline and surface-deep gradients are smaller. First, the change in the overall $\delta^{13}C$
553 signature of weathering carbon input does not change by the same absolute amount for
554 an increase and decrease in organic input. A 40% decrease in organic input changes the
555 overall $\delta^{13}C$ signature of weathering carbon input by ~2 ‰, while a 40% increase changes
556 it by ~3 ‰. The initial perturbation in $\delta^{13}C_{DIC}$ caused by the changed input is thus
557 smaller for an increase than a decrease (c.f. Fig. 5d-f). Second, while for a 40% decrease
558 in organic input, the POM export flux is reduced by about ~23%, in the case of a 40%
559 increase the POM export flux increases by only ~13%, thus affecting surface-thermocline
560 and surface-deep gradients differently. This non-linearity in the carbon isotopic response
561 has to be kept in mind, when interpreting proxy records in light of these step-change ex-
562 periments.

Sensitivity Experiment for Sedimentary P Leaching

564 Next, we turn to the results from the sensitivity experiment with idealized higher phos-
565 phate leaching from sediments (dashed lines in Fig. 4). 30% of the P in organic matter
566 leaving the ocean is immediately "leached back" to the water column. In this model setup,
567 the steady-state input flux of P is reduced in comparison to the standard run (Fig. 4a,
568 solid vs dashed line).

569   Generally, the response to a reduction in the organic input flux is amplified in the
570 case of the sensitivity experiment. In particular, the reduction in atmospheric CO_2 is
571 30% larger than in the standard model setup, as are the peak perturbations in $\delta^{13}C$ of
572 DIC and CO_2 around 20 kyr. The 40% reduction in the organic input flux translates into
573 a smaller absolute change in input in the sensitivity compared to the standard run, be-
574 cause the steady-state input flux of P is smaller (Fig. 4a). In turn, P limitation for ma-
575 rine biological production is less severe in the sensitivity experiment. This results in slightly
576 less reduced export fluxes of organic matter and $CaCO_3$, as compared to the standard
577 run (Fig. 4l), translating into temporarily higher net ocean-sediment loss fluxes (Fig. 4m;
578 dashed vs solid lines). The higher loss of POC and $CaCO_3$ causes DIC (and to a lesser
579 extent ALK) and CO_2 to decrease more in the sensitivity than standard setup.

580   Differences in the isotopic perturbation can be readily understood from differences
581 in the burial-input fluxes and an even further reduced fractionation during marine pho-

tosynthesis owing to the lower CO_2 concentration (see Table 1 and Fig. 4e,m-o). The majority of the carbon isotopic perturbation is again driven by the POC cycle (cf. Fig. 2c-d). The burial-input imbalance in the POC cycle is larger in the sensitivity experiment with preferential phosphate leaching from sediments, as compared to the standard organic input step-change experiment. This leads to an amplified increase in the δ^{13}C signature of the reactive carbon pools (see the larger perturbation in δ^{13}C in Fig. 4n,o). At the same time, lower atmospheric CO_2 and thus lower $[CO_{2,aq}]$ lead to less fractionation during marine photosynthesis and an increase in δ^{13}C of the POC burial flux. In total, this leads to initially higher positive δ^{13}C values in the atmosphere and ocean for the sensitivity experiment with subsequent declines in differences (Fig. 4n; 6b,d).

3.3 Scalability of Step-change Responses

Here, we address the linearity of responses in carbon and carbon isotopes to step-changes of different magnitudes (Fig. 6). In a linear system, the responses shown in Fig. 1 and 4 would be independent of the magnitude of the step-change. Then, the impact of any evolution of changes in $CaCO_3$ or organic matter input could be exactly described with the help of the responses or Green's functions shown in Fig. 1 and 4. While the carbon cycle is known to be non-linear, near-linear behavior may still emerge within certain limits of change. In Fig. 6 we compare the responses in CO_2, DIC, and their δ^{13}C signatures from eight step-change simulations where $CaCO_3$ or organic matter input was changed at nominal time $t=0$ over a wide range (-80% to +80%). All responses are normalized to a step increase in $CaCO_3$ or decrease in organic matter input of 40% for comparison with the experiments discussed above. The responses for steps within $\pm$ 40% are visually highlighted and linked by blue (for $CaCO_3$) and red (for organic matter) shading. The responses for larger step changes are not further discussed.

Generally, linearity is higher for step-changes in the $CaCO_3$ input as compared to organic matter input. Changes in DIC, $\delta^{13}C_{atm}$, and $\delta^{13}C_{DIC}$ are near-linear in the case of step-changes in $CaCO_3$ input, although non-linearities increase somewhat with time by up to $\pm$ 14-16% relative to the overall change at 100 kyr (Fig. 6b,c,d). The largest uncertainties are associated with the response in CO_2, where the mean response is -39 ppm, with a spread of $\pm$ 7 ppm ($\pm$ 18%) after 100 kyr and the range between +40% and -40% $CaCO_3$ input. The response in CO_2 is larger for a reduction than an increase in $CaCO_3$ input of equal magnitude (Fig. 6a). For step-changes in the organic input, near linearity is found for changes in DIC (spread: $\pm$ 7%) and, to a lesser extent, for atmospheric CO_2 ($\pm$7 ppm, $\pm$ 14%), $\delta^{13}C_{atm}$ ($\pm$ 20% relative to peak change), while the spread covers 0.2 ‰ ($\pm$ 37% relative to peak change) for $\delta^{13}C_{DIC}$ after 100 kyr and the range between +40% and -40% organic matter input.

In summary, the assumption of a near-linear response appears reasonable for changes in organic matter and $CaCO_3$ input within $\pm$40% around the mean state. Thus, the response functions displayed in Fig. 1and 4 broadly characterize the response to changes in $CaCO_3$ and organic matter input, enabling the construction of a simple emulator to simulate responses to time-varying input in a cost-efficient and transparent way as done in section 4.2.

4 Discussion

State-of-the-art Earth System Models or Earth System Models of Intermediate Complexity that explicitly represent processes on a 3-dimensional spatial grid and sub-annual time scales are computationally too expensive for simulations exceeding millions of years. However, the characteristic spatio-temporal responses of such complex models may be used to build cost-efficient substitute models (section 2.3) that account for the underlying spatio-temporal complexity of the involved processes. In the future, such models may also include spatially explicit weathering or ice sheets. The Green's response func-
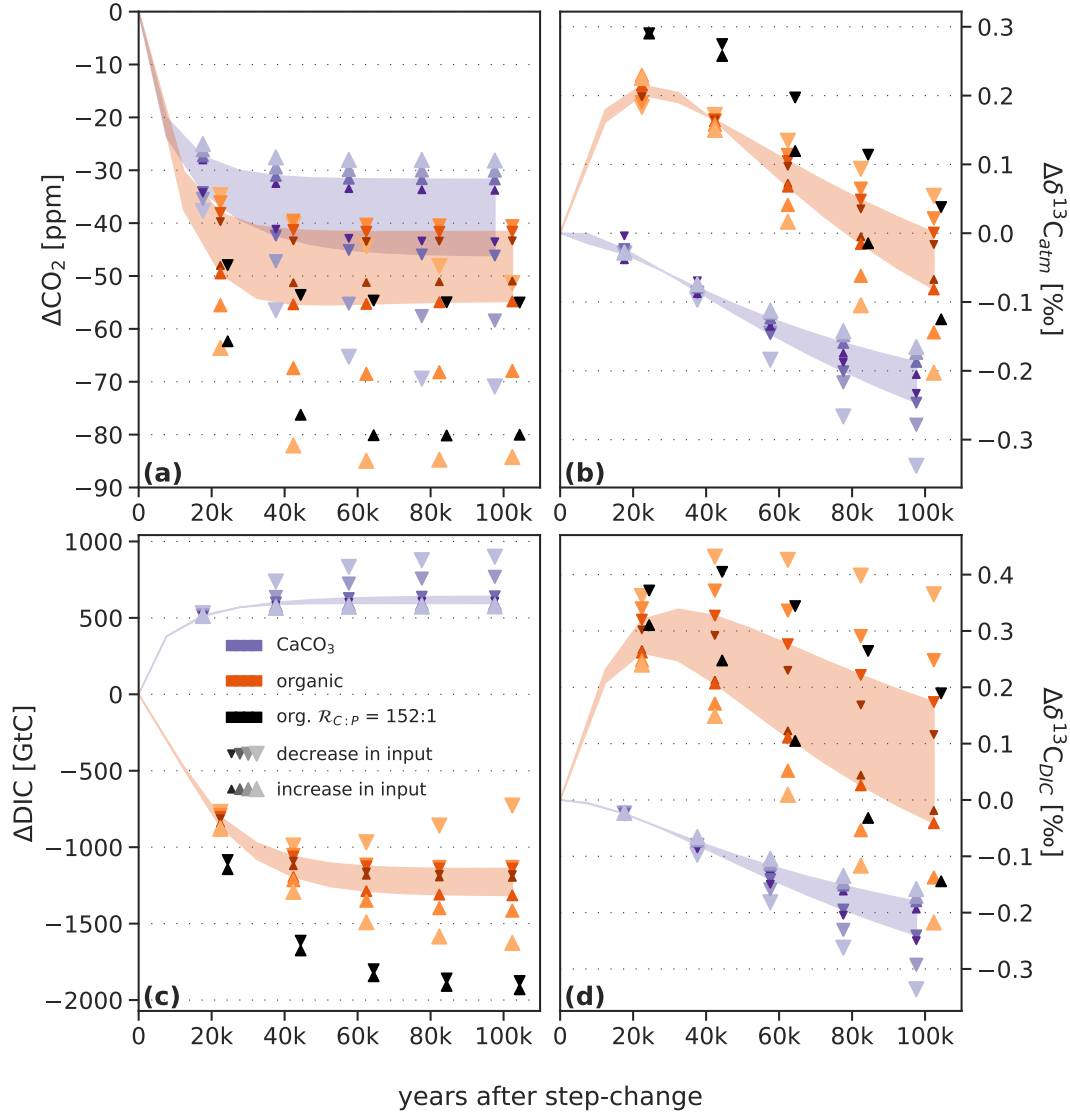
Figure 6. Normalized response functions. Change in (a) CO_2, (b) $\delta^{13}C_{atm}$, (c) DIC, and (d) $\delta^{13}C_{DIC}$ to step-changes in the input of $CaCO_3$ (blue), organic material (red), and organic material with a different C:P ratio (black, see section 2.2) at different times. Step-changes range from -80 to 80% in 20% increments (size of the markers). Results are scaled to an increase of 40% in case of $CaCO_3$ and a decrease of 40% in case of organic material. Red and blue envelops indicate the range from +40% to -40% of changes in $CaCO_3$ and organic input. Triangles are slightly offset in x-direction for visibility and black triangles show results only for an in-/decrease of 40% in the organic input flux.

tions from the Bern3D Earth System Model of Intermediate Complexity for changes in the net input of organic matter and $CaCO_3$ may also be viewed as a first step towards bringing spatial scales to modelling the carbon cycle over periods of many millions of years. In such long simulations, the atmosphere, ocean, land biosphere, and interactive sediments are usually taken as single reservoirs which differs from our approach, as we here explicitly consider the transfer of carbon, alkalinity, and phosphorus between these reservoirs and within the ocean.

The response timescales and amplitudes to perturbations in the input from the lithosphere are governed by the interplay between ocean circulation and air-sea exchange, nutrient transport to the ocean surface, marine biological productivity and the export of biogenic particles, and remineralization and redissolution of biogenic particles within the water column and sediments. Spatial gradients within the ocean and ocean sediments are important. For example, the removal rate of $\delta^{13}C$ perturbations is significantly modified by $\delta^{13}C$ gradients within the ocean, influencing the isotopic composition of the burial flux of organic and $CaCO_3$ particles in the lithosphere (Jeltsch-Thömmes & Joos, 2020).

The long timescales and the spatial complexity associated with burial-input imbalances and the carbon cycle is a challenge when investigating the glacial-interglacial variations of the past few million years. Box models may not capture spatial gradients, whereas glacial-interglacial simulations are computationally too expensive with weathering-sediment-enabled Earth System Models (Lacroix et al., 2020) and are even demanding for Earth System Models of Intermediate Complexity (e.g. Menviel et al., 2012; Colbourn et al., 2013; Ganopolski & Brovkin, 2017; Willeit et al., 2022). Cost-efficient substitute models, representing faithfully the response of spatially-resolved models, provide an alternative.

In brief, evaluating the response to a step-like change reveals underlying system dynamics and spatio-temporal response characteristics. This is useful for model-model comparison and for understanding the model responses to a perturbation. Further, the response can be used to build a cost-efficient substitute model (or emulator) to explore different forcing histories over long time scales (see section 4.2).

4.1 Uncertainties and Limitations

We apply an Earth system model of intermediate complexity. The use of the Bern3D model enables us to conduct 600 kyr long simulations considering fluid dynamics and biogeochemical processes in a spatially-resolved 3-dimensional setting. This is a progress compared to box models or 2-dimensional ocean models, typically applied for such long time scales. However, many processes are still represented by simplified parameterizations and some of these, as, for example, the dissolution rate constants in the marine sediments or the remineralization of organic matter in the water column, rely on global uniform parameter choices.

Another limitation relates to the stoichiometric ratios used in the model. The question of the C:P ratio in marine sediments and preferential P leaching to the ocean is discussed in the literature (e.g., Ingall & Jahnke, 1994; Delaney, 1998; L. D. Anderson et al., 2001). Under low oxygen conditions, for example, P is preferentially regenerated from marine sediments, (e.g., Ingall & Jahnke, 1994). This could lead to a positive feedback loop where more P is brought to the ocean surface enhancing primary production and organic matter export, and, in turn, enhancing organic matter transport to and remineralization at depth, further depleting bottom water oxygen through consumption of oxygen during remineralization (e.g., Van Cappellen & Ingall, 1994; Wallmann, 2010; Palastanga et al., 2011; Niemeyer et al., 2016; Watson, 2016; Kemena et al., 2019). Release of additional P from sediments could have a strong impact on $\delta^{13}C$ (see e.g., Tschumi et al., 2011, for a step-increase in the ocean's P inventory). In the current setup of the Bern3D model, we assume constant Redfield ratios in the ocean and sediment. Further,

in the standard step-change experiment of the organic input flux, the same constant C:P ratio of 117:1 is applied. To address this limitation, we conducted an additional experiment, where 30% of the P entering marine sediments in the model is immediately released back to the ocean (see section 2.1). While the quantitative results differ, the qualitative response is similar for the experiment with and without this idealized enhanced P leaching. Model formulations could be revised in the future for varying C:P ratios, preferential P leakage from sediments under low oxygen concentrations as done in the HAMOCC and UVic models (e.g., Palastanga et al., 2011; Niemeyer et al., 2016; Kemena et al., 2019), and variable stoichiometric ratios for biological production, e.g., Matsumoto et al. (2020). Lacroix et al. (2020) further discuss the question of C:P ratios of riverine weathering input of organic material. While terrestrial dissolved organic matter exhibits very high C:P ratios of up to 2583:1 (Meybeck, 1982; Compton et al., 2000), the ratio is uncertain in particulate organic matter (POM), with a range of 56-499 (Meybeck, 1982; Ramirez & Rose, 1992; Compton et al., 2000). In the experiments here, weathering of terrestrial dissolved organic material is not considered and the input flux F_{org} is assumed to originate from previously buried organic matter. In line with Lacroix et al. (2020), the C:P ratio of this F_{org} flux from the litosphere is the same as of oceanic POM.

For the evolution of δ^{13}C, the organic matter cycle and fractionation during marine photosynthesis plays an important role. Here, this fractionation is described using the empirical relationship with dissolved CO_2 by Freeman and Hayes (1992). Additionally, there are other environmental factors besides dissolved CO_2 that might affect fractionation during marine photosynthesis (Goericke & Fry, 1994). Jahn et al. (2015) implemented three parameterizations in their ocean model. One where fractionation varies with dissolved CO_2 and two also considering phytoplankton growth rates. Overall, all three parameterizations lead to the expected pattern of high δ^{13}C$_{DIC}$ in surface waters and low δ^{13}C$_{DIC}$ values in water that has been out of contact with the atmosphere for a long time. Liu et al. (2021) found good δ^{13}C data-model agreement for discrimination varying with dissolved CO_2 according to Popp et al. (1989), while the agreement was less favorable with a parameterization additionally varying with local phytoplankton growth rates (Laws et al., 1995). These findings lend indirect justification for applying the parameterization of Freeman and Hayes (1992), which is similar to that of Popp et al. (1989). While the application of alternative parameterizations would somewhat affect the quantitative findings of this study, the main messages would likely remain unchanged.

4.2 Scenarios for the past 800,000 years: Application of the Green's Function Substitute Model

We apply the Green's function emulator (Eq. 9; section 2.3) to easily investigate different scenarios for changes in $CaCO_3$ weathering and organic matter input over the past 800,000 years. We use the mean of the normalized responses to the +40 and -40% step-change in input for $CaCO_3$ and organic matter, respectively. This emulator is an approximation and non-linear interactions with carbon cycle changes other than those related to changes in weathering input are not taken into account. The aim of this exercise is not to provide conclusive answers how past changes in input fluxes affected atmospheric CO_2 and the carbon cycle, but rather to illustrate the usefulness of the Green's function approach to explore different scenarios and hypotheses.

In the first scenario, we apply the 0-dimensional version of the RokGeM v0.9 model (Colbourn et al., 2013) where $CaCO_3$ input is a function of atmospheric CO_2 (Bereiter et al., 2015) and global mean surface air temperature (SAT). SAT evolution is computed by linearly scaling the Antarctic temperature reconstruction of Jouzel et al. (2007)), assuming a difference in SAT between preindustrial (PI) and Last Glacial Maximum (LGM) of 5.5 K. RokGeM yields $CaCO_3$ weathering to be about 40% lower at LGM than PI (Fig. 7, turquoise). This is in contrast to Börker et al. (2020) who suggest $CaCO_3$ weathering to be about 30% higher at LGM than PI. In our second scenario, we linearly scale
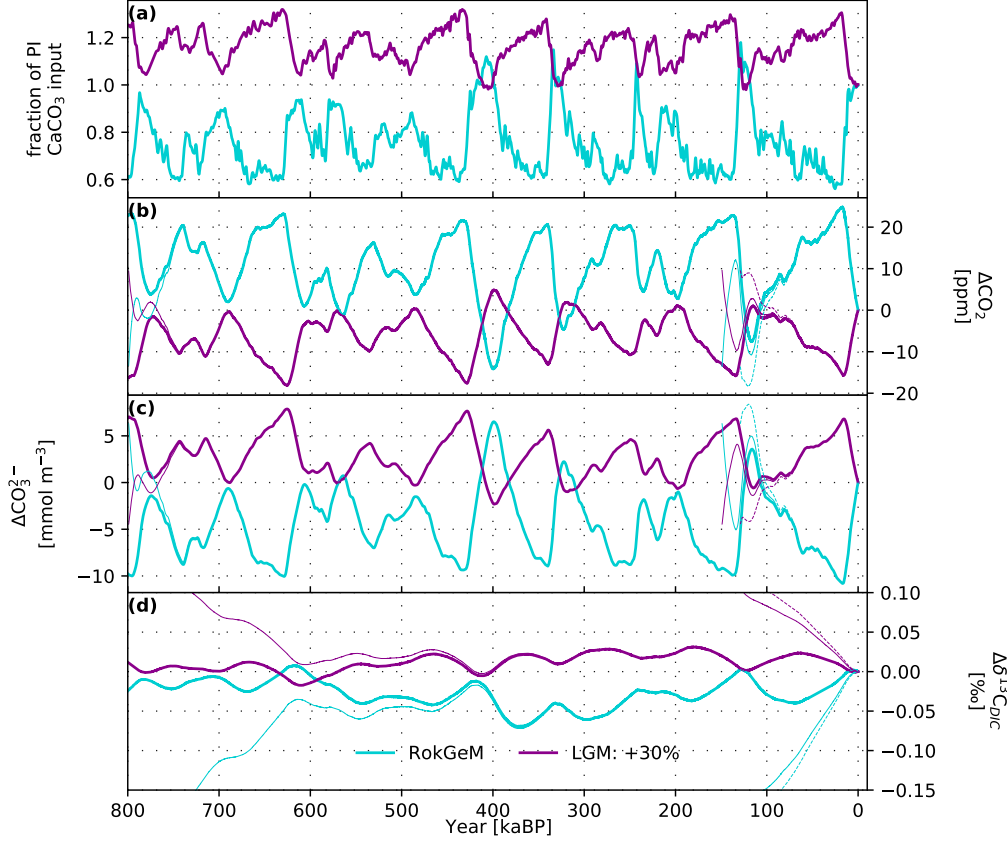
Figure 7. Two contrasting literature-based CaCO₃ weathering scenarios. (a) Prescribed changes in CaCO₃ weathering input (magenta: +30% in LGM, based on reconstructions of CaCO₃ weathering by Börker et al. (2020) and scaled with δ^{18}O (Lisiecki & Raymo, 2005); Turquoise: as calculated with the Rock Geochemical Model RokGeM v0.9 (Colbourn et al., 2013), where maximum LGM cooling of 5.5 K is scaled with the Antarctic temperature reconstruction by Jouzel et al. (2007)). Changes (relative to PI) in (b) atmospheric CO₂, (c) global mean CO_3^{2-}, and (d) global mean $\delta^{13}C_{DIC}$ as emulated using the responses of the step-change experiment. The first glacial cycles was repeated twice before starting the standard run at 800 kyr (thick lines). Sensitivity simulations, illustrating the drift associated with a "old start", were started directly at at 800, 150, and 130 kaBP (thin lines); results show that initial conditions affect simulated CO₂ for several ten thousand years and δ^{13}C for several hundred thousand years.

the δ^{18}O record of Lisiecki and Raymo (2005) to yield an LGM-PI difference of +30% in CaCO$_3$ input.

The scenario based on Börker et al. (2020) yields LGM minima of up to ∼15 ppm lower than at PI. In contrast, the scenario based on RokGem yields up to more than 20 ppm higher CO$_2$ during glacials (Fig. 7a,b). Overall, differences between the two literature-based scenarios are up to 35 ppm or about a third of the glacial-interglacial CO$_2$ amplitude. Similarly, changes in CO$_3^{2-}$ are opposite and differences between the two scenarios are up to 18 mmol m^{-3}. Generally, CO$_2$ and CO$_3^{2-}$ follow changes in weathering without much delay and capture some multi-millennial features of the forcing, while δ^{13}C$_{\text{DIC}}$ shows a strongly smoothed signal. Variations in δ^{13}C$_{\text{DIC}}$ are on the order < 0.05 ‰ and the timing of maxima/minima does not directly mirror changes in the forcing (Fig. 7d).

In the third scenario, we adopt the "shelf-weathering" hypothesis by Wallmann et al. (2016), where input of organic-derived material to the ocean is elevated during periods of low sea level. Taking their PI-LGM change at face value (see panel (h), Fig. 3 in Wallmann et al., 2016) translates into a ∼10% change of the total organic input in the Bern3D model. This PI-LGM difference in forcing is then scaled with δ^{18}O (Lisiecki & Raymo, 2005) to yield a forcing history of the past 800 kyr (Fig. 8a). This yields CO$_2$ changes of up to ∼10 ppm with higher CO$_2$ during glacials than interglacials (Fig. 8b). Changes in δ^{13}C$_{\text{DIC}}$ are on the order of 0.05 ‰ with lower values during glacials. This means that about 15% of the observed PI-LGM δ^{13}C$_{\text{DIC}}$ change (C. D. Peterson et al., 2014) could be attributed to changes in input from shelves. Contrary to changes in the CaCO$_3$ weathering, the signal in $\Delta\delta^{13}$C$_{\text{DIC}}$ is less smoothed and the timing reflects the forcing history (Fig. 8a,d). This is likely a results from the initial strong perturbation in δ^{13}C$_{\text{DIC}}$ resulting from changes in the input δ^{13}C signature (see Fig. 3n, 5d-f and section 3.2).

4.3 How to Initialize Earth System Models: The Glacial-Interglacial Cold Start Problem

The long adjustment timescales of carbon and δ^{13}C to perturbations in input-burial imbalances pose a serious challenge for model initialisation. Initial conditions affect the evolution of CO$_2$ and δ^{13}C over several ten thousand and hundred thousand years, respectively. In the standard setup of the emulator, the forcing history of the first glacial cycle is repeated twice, before starting the simulation at the nominal year 800 kaBP. We illustrate the impact and potential biases of such a "cold start" (Hasselmann et al., 1993) by starting the emulator at 800 kaBP, the beginning of our scenarios, at 150 kaBP, i.e. close to glacial maximum conditions, and at 130 kaBP, near the beginning of the last interglacial.

The initial trends in CO$_2$ and CO$_3^{2-}$ deviate strongly from standard results during many millennia (thin versus thick lines in Fig. 7) for all three sensitivity runs. This initial drift obscures the signals found in the standard run. For δ^{13}C, deviations extend as expected over several hundred thousand years. Results for δ^{13}C of the simulations started at 150 and 130 kaBP are useless and highly misleading. The simulated trend is about four times larger than the signal simulated in the standard setup.

The initial adjustment after a cold start is an intrinsic property of the Earth system as implemented in the parent Bern3D model (see Figs 1 and 4) and inherited by the emulator. The results highlight that models used to simulate the last deglacial or glacial-interglacial cycles and featuring input and burial fluxes must be carefully initialised to avoid wrong results and interpretations.
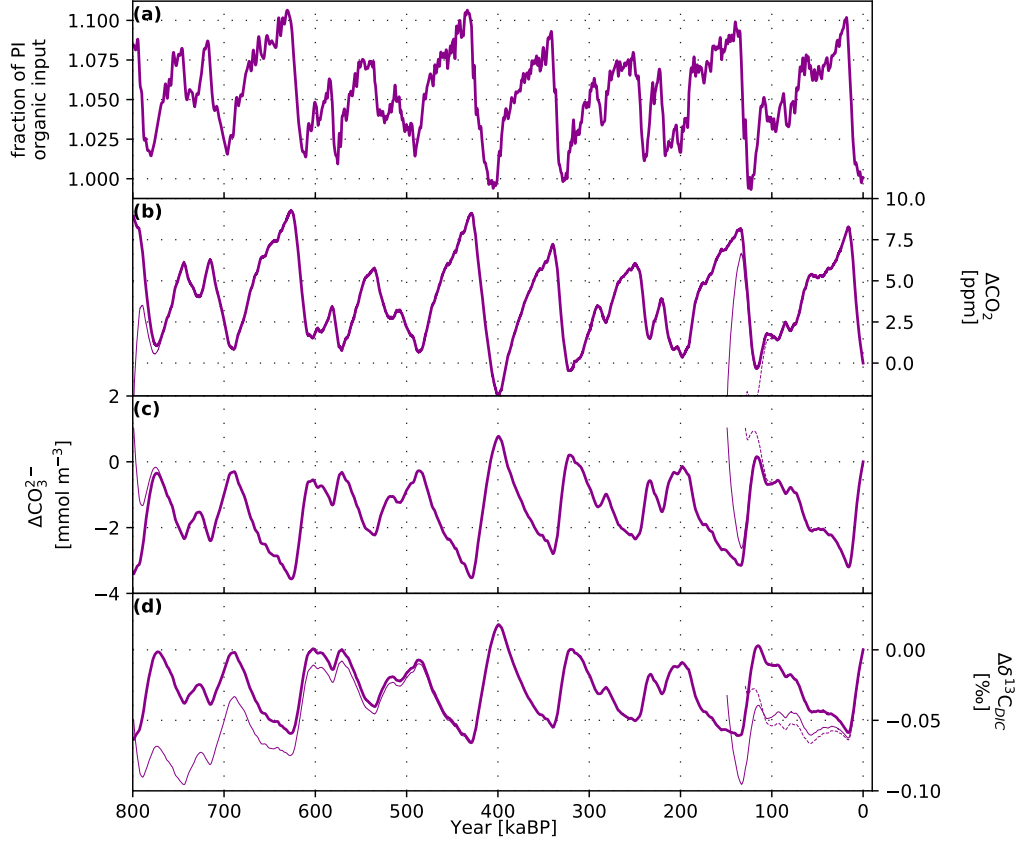
Figure 8. As Fig. 7 but for a scenario with varying input of organic-derived material (P:C:ALK=1:117:-17 and δ^{13}C=-20.42 ‰), based on (Wallmann, 2014; Wallmann et al., 2016)

5 Summary and Conclusions

We conducted idealized simulations applying a step-change in the input fluxes of DIC, ALK, P, and δ^{13}C from the lithosphere to the ocean. We assumed step changes in a conceptual input flux releasing the elements of former organic matter (F_{org}; P:ALK:DIC=1:-17:-117 with δ^{13}C=-20.42 ‰) or from $CaCO_3$ weathering (F_{CaCO_3}; ALK:DIC=2:1 with δ^{13}C=2.88 ‰). We analyzed the response in atmospheric CO_2, marine parameters (DIC, ALK, CO_3^{--}, pH, saturation horizon, export production), sedimentary and burial fluxes, and in δ^{13}C of various carbon reservoirs and fluxes in the Bern3D model. The two standard simulations extend over 600,000 years and F_{CaCO_3} is increased by 40% and F_{org} reduced by 40%, respectively.

Atmospheric CO_2 decreased exponentially by about 30 ppm in both simulations. The e-folding adjustment time scale for CO_2 and other carbon cycle parameters is ∼7,500 years for the step change in F_{org} and ∼9,900 years for the step in F_{CaCO_3}. The difference in time scales reflects differences in underlying processes. While sedimentary $CaCO_3$ compensation is the controlling process after a change in $CaCO_3$ weathering, a reduction in organic matter export and burial and the marine phosphorus inventory govern the carbon response after the reduction in F_{org} and P input to the ocean.

For the increase in F_{CaCO_3}, δ^{13}C of atmospheric CO_2, DIC, and $CaCO_3$ decreases gradually with a time scale of ∼57,300 years to stabilize 0.35‰ lower than before the step in F_{CaCO_3}. The adjustment in δ^{13}C is controlled by burial-input imbalances in both the cycling of $CaCO_3$ and organic matter. The decrease in CO_2 in the surface ocean causes less fractionation during photosynthesis and an increase in δ^{13}C of organic matter. In turn, a larger burial of δ^{13}C is mediated by organic matter burial which is at the new equilibrium compensated by an opposite perturbation in the δ^{13}C removal by $CaCO_3$ burial.

For the reduction in F_{org}, δ^{13}C of atmospheric CO_2, DIC and $CaCO_3$ increases initially by about 0.3‰. This increase is in response to the reduced input of isotopically light carbon and follows a time scale of about ∼5,800 years. At peaking, the reduced input is compensated by a reduced burial of organic matter. Afterward, δ^{13}C decreases with an adjustment time scale of ∼110,000 to stabilize only after several hundred thousand years. This decrease is, similar as for the change in $CaCO_3$ weathering, related to the positive shift in δ^{13}C of marine organic matter due to lower CO_2. The reduction in the export and the remineralization fluxes of organic matter and their changes in isotopic signature cause distinct spatial patterns within the ocean. The surface-to-thermocline gradient is reduced by about 0.25‰.

The application of a step change in input allows for probing the so-called Green's function response. The normalized responses are used to build a simple, cost-efficient emulator. Simulating one million years takes a few seconds with the emulator, while it would take about three months using Bern3D. The emulator is applied in a range of literature-based scenarios for the past 800,000 years to estimate carbon cycle changes to plausible time-varying input fluxes from the lithosphere or shelves. These reveal differences in simulated CO_2 of up to a third of the reconstructed glacial-interglacial amplitude, and differences in CO_3^{--}, and small (0.05 to 0.1 ‰), but non-negligible, changes in δ^{13}C. Our emulator, is probably most useful for periods with a close-to-modern continental configuration. However, Green's function emulators could also be valuable for studying Earth's long history.

The long adjustment time scales of ten thousand years, and even a hundred thousand years for δ^{13}C, pose a serious challenge for sediment-enabled model simulations. The model needs to be initialized carefully to avoid model drift obscuring the responses to any applied forcing, rendering results misleading and useless, as exemplified in cold-start simulations with the emulator.

834   Our results highlight the importance to consider weathering–burial (input–output)
835   imbalances and interactions between the atmosphere-ocean-land biosphere system and
836   reactive ocean sediments in modeling studies that investigate CO_2 and $\delta^{13}C$ on multi-
837   millennial and longer timescales. A thorough understanding of the mechanisms affect-
838   ing atmospheric CO_2, $\delta^{13}C_{DIC}$, CO_3^{2-} and other carbon cycle parameters will help in the
839   interpretation of paleo-records. Already small imbalances in the burial-input cycle can
840   have large effects on carbon and carbon isotopes in the Earth system and are thus likely
841   candidates to have contributed to the reconstructed glacial-interglacial variations.

Acknowledgments

Data used for the figures and necessary for construction of the emulator will be made available upon peer-review completion on zenodo.org and accessible via doi. Additional data is available upon request from the corresponding author. During peer-review, data can be accessed under the following share-link: `https://cloud.climate.unibe.ch/s/nfGTZRmkrs5SAyF`

The authors declare that they have no conflict of interest.

References

Anderson, L. A., & Sarmiento, J. L. (1994). Redfield ratios of remineralization determined by nutrient data analysis. *Global Biogeochemical Cycles*, *8*(1), 65–80. Retrieved from `https://agupubs.onlinelibrary.wiley.com/doi/abs/10.1029/93GB03318` doi: 10.1029/93GB03318

Anderson, L. D., Delaney, M. L., & Faul, K. L. (2001). Carbon to phosphorus ratios in sediments: Implications for nutrient cycling. *Global Biogeochemical Cycles*, *15*(1), 65–79. Retrieved from `http://doi.wiley.com/10.1029/2000GB001270` doi: 10.1029/2000GB001270

Archer, D., Kheshgi, H., & Maier-Reimer, E. (1997). Multiple timescales for neutralization of fossil fuel CO_2. *Geophysical Research Letters*, *24*(4), 405–408. doi: 10.1029/97GL00168

Archer, D., Kheshgi, H., & Maier-Reimer, E. (1998). Dynamics of fossil fuel CO_2 neutralization by marine CaCO3. *Global Biogeochemical Cycles*, *12*(2), 259–276. doi: 10.1029/98GB00744

Archer, D., & Maier-Reimer, E. (1994). Effect of deep-sea sedimentary calcite preservation on atmospheric CO_2 concentration. *Nature*, *367*(6460), 260–263. doi: 10.1038/367260a0

Archer, D., Winguth, A., Lea, D., & Mahowald, N. (2000). What caused the glacial/interglacial atmospheric pCO_2 cycles? *Reviews of Geophysics*, *38*(2), 159–189.

Bastiaansen, R., Dijkstra, H. A., & Heydt, A. S. v. d. (2021). Projections of the Transient State-Dependency of Climate Feedbacks. *Geophysical Research Letters*, *48*(20), e2021GL094670. Retrieved from `https://agupubs.onlinelibrary.wiley.com/doi/abs/10.1029/2021GL094670` (e2021GL094670 2021GL094670) doi: https://doi.org/10.1029/2021GL094670

Battaglia, G., Steinacher, M., & Joos, F. (2016). A probabilistic assessment of calcium carbonate export and dissolution in the modern ocean. *Biogeosciences*, *13*(9), 2823–2848. doi: 10.5194/bg-13-2823-2016

Bereiter, B., Eggleston, S., Schmitt, J., Nehrbass-Ahles, C., Stocker, T. F., Fischer, H., . . . Chappellaz, J. (2015). Revision of the EPICA Dome C CO_2 record from 800 to 600 kyr before present. *Geophysical Research Letters*, *42*(2), 542–549. doi: 10.1002/2014GL061957

Bergman, N., Lenton, T., & Watson, A. (2004). COPSE: A new model of biogeochemical cycling over Phanerozoic time. *American Journal of Science*, *304*(5), 397-437. doi: 10.2475/ajs.304.5.397

Berner, R. A. (1990). Atmospheric Carbon Dioxide Levels Over Phanero-

zoic Time. *Science*, *249*(4975), 1382-1386. Retrieved from `https://www.science.org/doi/abs/10.1126/science.249.4975.1382` doi: 10.1126/science.249.4975.1382

Berner, R. A. (2006). GEOCARBSULF: A combined model for Phanerozoic atmospheric O_2 and CO_2. *Geochimica et Cosmochimica Acta*, *70*(23), 5653-5664. Retrieved from `https://www.sciencedirect.com/science/article/pii/S0016703706002031` (A Special Issue Dedicated to Robert A. Berner) doi: https://doi.org/10.1016/j.gca.2005.11.032

Broecker, W. S. (1970). A boundary condition on the evolution of atmospheric oxygen. *Journal of Geophysical Research (1896-1977)*, *75*(18), 3553-3557. Retrieved from `https://agupubs.onlinelibrary.wiley.com/doi/abs/10.1029/JC075i018p03553` doi: https://doi.org/10.1029/JC075i018p03553

Broecker, W. S., & Peng, T.-H. (1987). The role of CaCO3 compensation in the glacial to interglacial atmospheric CO_2 change. *Global Biogeochemical Cycles*, *1*(1), 15–29. doi: 10.1029/GB001i001p00015

Broecker, W. S., & Peng, T.-H. (1989). The cause of the glacial to interglacial atmospheric CO_2 change: A polar alkalinity hypothesis. *Global Biogeochemical Cycles*, *3*(3), 215–239.

Brovkin, V., Ganopolski, A., Archer, D., & Munhoven, G. (2012). Glacial CO_2 cycle as a succession of key physical and biogeochemical processes. *Climate of the Past*, *8*(1), 251–264. doi: 10.5194/cp-8-251-2012

Börker, J., Hartmann, J., Amann, T., Romero-Mujalli, G., Moosdorf, N., & Jenkins, C. (2020). Chemical Weathering of Loess and Its Contribution to Global Alkalinity Fluxes to the Coastal Zone During the Last Glacial Maximum, Mid-Holocene, and Present. *Geochemistry, Geophysics, Geosystems*, *21*(7), e2020GC008922. Retrieved from `https://agupubs.onlinelibrary.wiley.com/doi/abs/10.1029/2020GC008922` (e2020GC008922 2020GC008922) doi: https://doi.org/10.1029/2020GC008922

Cartapanis, O., Bianchi, D., Jaccard, S., & Galbraith, E. D. (2016). Global pulses of organic carbon burial in deep-sea sediments during glacial maxima. *Nature communications*, *7*, 10796. doi: 10.1038/ncomms10796

Cartapanis, O., Galbraith, E. D., Bianchi, D., & Jaccard, S. L. (2018). Carbon burial in deep-sea sediment and implications for oceanic inventories of carbon and alkalinity over the last glacial cycle. *Climate of the Past*, *14*(11), 1819–1850. doi: 10.5194/cp-14-1819-2018

Caves, J. K., Jost, A. B., Lau, K. V., & Maher, K. (2016). Cenozoic carbon cycle imbalances and a variable weathering feedback. *Earth and Planetary Science Letters*, *450*, 152-163. doi: {10.1016/j.epsl.2016.06.035}

Clark, P. U., Archer, D., Pollard, D., Blum, J. D., Rial, J. A., Brovkin, V., ... Roy, M. (2006). The middle Pleistocene transition: characteristics, mechanisms, and implications for long-term changes in atmospheric pCO$_2$. *Quaternary Science Reviews*, *25*(23-24), 3150–3184. doi: 10.1016/j.quascirev.2006.07.008

Colbourn, G., Ridgwell, A., & Lenton, T. M. (2013). The Rock Geochemical Model (RokGeM) v0.9. *Geoscientific Model Development*, *6*(5), 1543–1573. doi: 10.5194/gmd-6-1543-2013

Colbourn, G., Ridgwell, A., & Lenton, T. M. (2015). The time scale of the silicate weathering negative feedback on atmospheric CO_2. *Global Biogeochemical Cycles*, *29*(5), 583–596. doi: 10.1002/2014GB005054

Compton, J., Mallinson, D., Glenn, C., Filippelli, G., Föllmi, K., Shields, G., & Zanin, Y. (2000). Variations in the global phosphorus cycle. In *Marine Authigenesis: From Global to Microbial* (p. 21-33). Wiley-Blackwell.

Delaney, M. L. (1998). Phosphorus accumulation in marine sediments and the oceanic phosphorus cycle. *Global Biogeochemical Cycles*, *12*(4), 563–572. Retrieved from `http://doi.wiley.com/10.1029/98GB02263` doi: 10.1029/98GB02263

Edwards, N. R., Willmott, A. J., & Killworth, P. D. (1998). On the Role of Topography and Wind Stress on the Stability of the Thermohaline Circulation. *Journal of Physical Oceanography*, *28*(5), 756–778. doi: 10.1175/1520-0485(1998) 028⟨0756:OTROTA⟩2.0.CO;2

Eggleston, S., Schmitt, J., Bereiter, B., Schneider, R., & Fischer, H. (2016). Evolution of the stable carbon isotope composition of atmospheric CO_2 over the last glacial cycle. *Paleoceanography*, *31*(3), 434–452. doi: 10.1002/2015PA002874

Emerson, S., & Archer, D. (1992). Glacial carbonate dissolution cycles and atmospheric pCO_2: A view from the ocean bottom. *Paleoceanography*, *7*(3), 319–331. doi: 10.1029/92PA00773

Emerson, S., & Bender, M. (1981). Carbonate Fluxes at the Sediment-Water Interface of the Deep-Sea - Calcium-Carbonate Preservation. *Journal of Marine Research*, *39*(1), 139-162.

Feely, R. A., Sabine, C. L., Lee, K., Berelson, W., Kleypas, J., Fabry, V. J., & Millero, F. J. (2004). Impact of Anthropogenic CO_2 on the CaCO3 System in the Oceans. *Science*, *305*, 362–366.

Freeman, K. H., & Hayes, J. M. (1992). Fractionation of carbon isotopes by phytoplankton and estimates of ancient CO_2 levels. *Global Biogeochemical Cycles*, *6*(2), 185–198. doi: 10.1029/92GB00190

Ganopolski, A., & Brovkin, V. (2017). Simulation of climate, ice sheets and CO_2 evolution during the last four glacial cycles with an Earth system model of intermediate complexity. *Climate of the Past*, *13*(12), 1695–1716. doi: 10.5194/cp-13-1695-2017

Goericke, R., & Fry, B. (1994). Variations of marine plankton $\delta^{13}C$ with latitude, temperature, and dissolved CO_2 in the world ocean. *Global Biogeochemical Cycles*, *8*(1), 85-90. Retrieved from https://agupubs.onlinelibrary .wiley.com/doi/abs/10.1029/93GB03272 doi: https://doi.org/10.1029/ 93GB03272

Goodwin, P., & Ridgwell, A. (2010). Ocean-atmosphere partitioning of anthropogenic carbon dioxide on multimillennial timescales. *Global Biogeochemical Cycles*, *24*(2), GB2014,. Retrieved from http://doi.wiley.com/10.1029/ 2008GB003449 doi: 10.1029/2008GB003449

Griffies, S. M. (1998). The Gent–McWilliams Skew Flux. *Journal of Physical Oceanography*, *28*(5), 831–841. doi: 10.1175/1520-0485(1998)028⟨0831: TGMSF⟩2.0.CO;2

Hartmann, J., Moosdorf, N., Lauerwald, R., Hinderer, M., & West, A. J. (2014). Global chemical weathering and associated P-release - The role of lithology, temperature and soil properties. *Chemical Geology*, *363*, 145-163. doi: 10.1016/j.chemgeo.2013.10.025

Hasselmann, K., Sausen, R., Maier-Reimer, E., & Voss, R. (1993). On the cold start problem in transient simulations with coupled atmosphere-ocean models. *Climate Dynamics*, *9*(2), 53-61. doi: 10.1007/BF00210008

Hayes, J. M., & Waldbauer, J. R. (2006). The carbon cycle and associated redox processes through time. *Philosophical Transactions of the Royal Society B - Biological Sciences*, *361*(1470), 931-950. (Conference on Major Steps in Cell Evolution - Palaeontological, Molecular and Cellular Evidence of their Timing and Global Effects, Royal Soc, London, ENGLAND, SEP 26-27, 2005) doi: 10.1098/rstb.2006.1840

Heinze, C., Maier-Reimer, E., Winguth, A. M. E., & Archer, D. (1999). A global oceanic sediment model for long-term climate studies. *Global Biogeochemical Cycles*, *13*(1), 221–250. doi: 10.1029/98GB02812

Hoogakker, B. A., Rohling, E. J., Palmer, M. R., Tyrrell, T., & Rothwell, R. G. (2006). Underlying causes for long-term global ocean $\delta13C$ fluctuations over the last 1.20 Myr. *Earth and Planetary Science Letters*, *248*(1-2), 15–29. doi: 10.1016/j.epsl.2006.05.007

Hooss, G., Voss, R., Hasselmann, K., Maier-Reimer, E., & Joos, F. (2001). A nonlinear impulse response model of the coupled carbon cycle-climate system (NICCS). *Climate Dynamics*, *18*(3-4), 189–202. doi: 10.1007/s003820100170

Huybers, P., & Langmuir, C. (2009). Feedback between deglaciation, volcanism, and atmospheric CO_2. *Earth and Planetary Science Letters*, *286*(3-4), 479–491. doi: 10.1016/j.epsl.2009.07.014

Ingall, E., & Jahnke, R. (1994). Evidence for enhanced phosphorus regeneration from marine sediments overlain by oxygen depleted waters. *Geochimica et Cosmochimica Acta*, *58*(11), 2571–2575. Retrieved from https://linkinghub.elsevier.com/retrieve/pii/0016703794900337 doi: 10.1016/0016-7037(94)90033-7

Isson, T. T., Planavsky, N. J., Coogan, L. A., Stewart, E. M., Ague, J. J., Bolton, E. W., . . . Kump, L. R. (2020). Evolution of the Global Carbon Cycle and Climate Regulation on Earth. *Global Biogeochemical Cycles*, *34*(2). doi: 10.1029/2018GB006061

Jahn, A., Lindsay, K., Giraud, X., Gruber, N., Otto-Bliesner, B. L., Liu, Z., & Brady, E. C. (2015). Carbon isotopes in the ocean model of the Community Earth System Model (CESM1). *Geoscientific Model Development*, *8*(8), 2419–2434. Retrieved from https://gmd.copernicus.org/articles/8/2419/2015/ doi: 10.5194/gmd-8-2419-2015

Jeltsch-Thömmes, A., Battaglia, G., Cartapanis, O., Jaccard, S. L., & Joos, F. (2019). Low terrestrial carbon storage at the Last Glacial Maximum: constraints from multi-proxy data. *Climate of the Past*, *15*(2), 849–879. doi: 10.5194/cp-15-849-2019

Jeltsch-Thömmes, A., & Joos, F. (2020). Modeling the evolution of pulse-like perturbations in atmospheric carbon and carbon isotopes: the role of weathering-sedimentation imbalances. *Climate of the Past*, *16*(2), 423–451. Retrieved from https://www.clim-past.net/16/423/2020/ doi: 10.5194/cp-16-423-2020

Joos, F., & Bruno, M. (1996). Pulse response functions are cost-efficient tools to model the link between carbon emissions, atmospheric CO_2 and global warming. *Physics and Chemistry of The Earth*, *21*(5-6), 471–476. doi: 10.1016/S0079-1946(97)81144-5

Joos, F., Prentice, I. C., Sitch, S., Meyer, R., Hooss, G., Plattner, G.-k., . . . Hasselmann, K. (2001). Global warming feedbacks on terrestrial carbon uptake under the Intergovernmental Panel on Climate Change (IPCC) Emission Scenarios. *Global Biogeochemical Cycles*, *15*(4), 891–907. doi: 10.1029/2000GB001375

Joos, F., Roth, R., Fuglestvedt, J. S., Peters, G. P., Enting, I. G., Von Bloh, W., . . . Weaver, A. J. (2013). Carbon dioxide and climate impulse response functions for the computation of greenhouse gas metrics: A multi-model analysis. *Atmospheric Chemistry and Physics*, *13*(5), 2793–2825. doi: 10.5194/acp-13-2793-2013

Jouzel, J., Masson-Delmotte, V., Cattani, O., Dreyfus, G., Falourd, S., Hoffmann, G., . . . Wolff, E. W. (2007). Orbital and Millennial Antarctic Climate Variability over the Past 800,000 Years. *Science*, *317*(5839), 793–796. Retrieved from https://www.sciencemag.org/lookup/doi/10.1126/science.1141038 doi: 10.1126/science.1141038

Kalnay, E., Kanamitsu, M., Kistler, R., Collins, W., Deaven, D., Gandin, L., . . . Joseph, D. (1996). The ncep/ncar 40-year reanalysis project. *Bulletin of the American Meteorological Society*, *77*(3), 437 - 472. Retrieved from https://journals.ametsoc.org/view/journals/bams/77/3/1520-0477_1996_077_0437_tnyrp_2_0_co_2.xml doi: 10.1175/1520-0477(1996)077⟨0437:TNYRP⟩2.0.CO;2

Kasting, J. F. (2019). The Goldilocks Planet? How Silicate Weathering Maintains Earth "Just Right". *Elements*, *15*(4), 235-240. doi: 10.2138/gselements.15.4.235

Kemena, T. P., Landolfi, A., Oschlies, A., Wallmann, K., & Dale, A. W. (2019). Ocean phosphorus inventory: large uncertainties in future projections on millennial timescales and their consequences for ocean deoxygenation. *Earth System Dynamics*, *10*(3), 539–553. Retrieved from `https://www.earth-syst-dynam.net/10/539/2019/` doi: 10.5194/esd-10-539-2019

Komar, N., & Zeebe, R. E. (2021). Reconciling atmospheric co¡sub¿2¡/sub¿, weathering, and calcite compensation depth across the cenozoic. *Science Advances*, *7*(4), eabd4876. Retrieved from `https://www.science.org/doi/abs/10.1126/sciadv.abd4876` doi: 10.1126/sciadv.abd4876

Kump, L. R., & Alley, R. B. (1994). Global chemical weathering on glacial time scales. *Material Fluxes on the Surface of the Earth*, 46–60.

Köhler, P., & Munhoven, G. (2020). Late Pleistocene Carbon Cycle Revisited by Considering Solid Earth Processes. *Paleoceanography and Paleoclimatology*, *35*(12), e2020PA004020. Retrieved from `https://agupubs.onlinelibrary.wiley.com/doi/abs/10.1029/2020PA004020` (e2020PA004020 10.1029/2020PA004020) doi: https://doi.org/10.1029/2020PA004020

Lacroix, F., Ilyina, T., & Hartmann, J. (2020). Oceanic CO_2 outgassing and biological production hotspots induced by pre-industrial river loads of nutrients and carbon in a global modeling approach. *Biogeosciences*, *17*(1), 55-88. doi: 10.5194/bg-17-55-2020

Lacroix, F., Ilyina, T., Laruelle, G. G., & Regnier, P. (2021). Reconstructing the Preindustrial Coastal Carbon Cycle Through a Global Ocean Circulation Model: Was the Global Continental Shelf Already Both Autotrophic and a CO_2 Sink? *Global Biogeochemical Cycles*, *35*(2), e2020GB006603. Retrieved from `https://agupubs.onlinelibrary.wiley.com/doi/abs/10.1029/2020GB006603` (e2020GB006603 2020GB006603) doi: https://doi.org/10.1029/2020GB006603

Laws, E. A., Popp, B. N., Bidigare, R. R., Kennicutt, M. C., & Macko, S. A. (1995). Dependence of phytoplankton carbon isotopic composition on growth rate and $[CO_{2,aq}]$: Theoretical considerations and experimental results. *Geochimica et Cosmochimica Acta*, *59*(6), 1131-1138. Retrieved from `https://www.sciencedirect.com/science/article/pii/0016703795000304` doi: https://doi.org/10.1016/0016-7037(95)00030-4

Lisiecki, L. E. (2014). Atlantic overturning responses to obliquity and precession over the last 3 Myr. *Paleoceanography*, *29*(2), 71-86. Retrieved from `https://agupubs.onlinelibrary.wiley.com/doi/abs/10.1002/2013PA002505` doi: https://doi.org/10.1002/2013PA002505

Lisiecki, L. E., & Raymo, M. E. (2005). A Pliocene-Pleistocene stack of 57 globally distributed benthic d18O records. *Paleoceanography*, *20*(1), 1–17. doi: 10.1029/2004PA001071

Liu, B., Six, K. D., & Ilyina, T. (2021). Incorporating the stable carbon isotope ^{13}C in the ocean biogeochemical component of the Max Planck Institute Earth System Model. *Biogeosciences*, *18*(14), 4389–4429. Retrieved from `https://bg.copernicus.org/articles/18/4389/2021/` doi: 10.5194/bg-18-4389-2021

Lourantou, A., Chappellaz, J., Barnola, J. M., Masson-Delmotte, V., & Raynaud, D. (2010). Changes in atmospheric CO_2 and its carbon isotopic ratio during the penultimate deglaciation. *Quaternary Science Reviews*, *29*(17-18), 1983–1992. doi: 10.1016/j.quascirev.2010.05.002

Lüthi, D., Le Floch, M., Bereiter, B., Blunier, T., Barnola, J. M., Siegenthaler, U., ... Stocker, T. F. (2008). High-resolution carbon dioxide concentration record 650,000-800,000 years before present. *Nature*, *453*(7193), 379–382. doi: 10.1038/nature06949

Maier-Reimer, E., & Hasselmann, K. (1987). Transport and storage of CO_2 in the

ocean - an inorganic ocean-circulation carbon cycle model. *Climate Dynamics*, *2*(2), 63–90. doi: 10.1007/BF01054491

Marcott, S. a., Bauska, T. K., Buizert, C., Steig, E. J., Rosen, J. L., Cuffey, K. M., ... Brook, E. J. (2014). Centennial-scale changes in the global carbon cycle during the last deglaciation. *Nature*, *514*(7524), 616–9. doi: 10.1038/nature13799

Matsumoto, K., Rickaby, R., & Tanioka, T. (2020). Carbon Export Buffering and CO_2 Drawdown by Flexible Phytoplankton C:N:P Under Glacial Conditions. *Paleoceanography and Paleoclimatology*, *35*(7), e2019PA003823. Retrieved from https://agupubs.onlinelibrary.wiley.com/doi/abs/10.1029/2019PA003823 (e2019PA003823 2019PA003823) doi: https://doi.org/10.1029/2019PA003823

Menviel, L., Joos, F., & Ritz, S. P. (2012). Simulating atmospheric CO_2, 13C and the marine carbon cycle during the Last Glacial-Interglacial cycle: Possible role for a deepening of the mean remineralization depth and an increase in the oceanic nutrient inventory. *Quaternary Science Reviews*, *56*, 46–68. doi: 10.1016/j.quascirev.2012.09.012

Metzler, H., Müller, M., & Sierra, C. A. (2018). Transit-time and age distributions for nonlinear time-dependent compartmental systems. *Proceedings of the National Academy of Sciences*, *115*(6), 1150-1155. Retrieved from https://www.pnas.org/doi/abs/10.1073/pnas.1705296115 doi: 10.1073/pnas.1705296115

Meybeck, M. (1982). Carbon, Nitrogen, ans Phosphorous Transport by World Rivers. *American Journal of Science*, *282*(4), 401-450. doi: 10.2475/ajs.282.4.401

Milliman, J. D., & Droxler, A. W. (1996). Neritic and pelagic carbonate sedimentation in the marine environment: Ignorance is not bliss. *Geologische Rundschau*, *85*(3), 496–504. doi: 10.1007/BF02369004

Mills, B. J. W., Scotese, C. R., Walding, N. G., Shields, G. A., & Lenton, T. M. (2017). Elevated CO_2 degassing rates prevented the return of Snowball Earth during the Phanerozoic. *Nature Communications*, *8*. doi: 10.1038/s41467-017-01456-w

Mook, W. G. (1986). 13C in atmospheric CO_2. *Netherlands Journal of Sea Research*, *20*(2-3), 211–223. doi: 10.1016/0077-7579(86)90043-8

Müller, S. A., Joos, F., Edwards, N. R., & Stocker, T. F. (2006). Water Mass Distribution and Ventilation Time Scales in a Cost-Efficient, Three-Dimensional Ocean Model. *Journal of Climate*, *19*(21), 5479–5499. doi: 10.1175/JCLI3911.1

Müller, S. A., Joos, F., Plattner, G. K., Edwards, N. R., & Stocker, T. F. (2008). Modeled natural and excess radiocarbon: Sensitivies to the gas exchange formulation and ocean transport strength. *Global Biogeochemical Cycles*, *22*(3), 1–14. doi: 10.1029/2007GB003065

Munhoven, G. (2002). Glacial - Interglacial changes of continental weathering: Estimates of the related CO_2 and HCO3 - flux variations and their uncertainties. *Global and Planetary Change*, *33*(1-2), 155–176. doi: 10.1016/S0921-8181(02)00068-1

Munhoven, G., & François, L. M. (1996). Glacial-interglacial variability of atmospheric CO_2 due to changing continental silicate rock weathering: A model study. *Journal of Geophysical Research: Atmospheres*, *101*(D16), 21423-21437. Retrieved from https://agupubs.onlinelibrary.wiley.com/doi/abs/10.1029/96JD01842 doi: https://doi.org/10.1029/96JD01842

Najjar, R. G., & Orr, J. C. (1999). *Biotic-HOWTO. Internal OCMIP* (Tech. Rep.). Saclay, Gif-sur-Yvette, France: LSCE/CEA.

Neftel, A., Oeschger, H., Schwander, J., Stauffer, B., & Zumbrunn, R. (1982). Ice core sample measurements give atmospheric CO_2 content during the past

40,000 yr. *Nature*, *295*(5846), 220–223. doi: 10.1038/295220a0

Niemeyer, D., Kemena, T. P., Meissner, K. J., & Oschlies, A. (2016). A model study of warming-induced phosphorus-oxygen feedbacks in open-ocean oxygen minimum zones on millennial timescales. *Earth System Dynamics Discussions*, 1–18. doi: 10.5194/esd-2016-50

Oliver, K. I. C., Hoogakker, B. A. A., Crowhurst, S., Henderson, G. M., Rickaby, R. E. M., Edwards, N. R., & Elderfield, H. (2010). A synthesis of marine sediment core d13C data over the last 150 000 years. *Climate of the Past*, *6*(5), 645–673. doi: 10.5194/cp-6-645-2010

Orr, J. C., & Epitalon, J. M. (2015). Improved routines to model the ocean carbonate system: Mocsy 2.0. *Geoscientific Model Development*, *8*(3), 485–499. doi: 10.5194/gmd-8-485-2015

Palastanga, V., Slomp, C. P., & Heinze, C. (2011). Long-term controls on ocean phosphorus and oxygen in a global biogeochemical model. *Global Biogeochemical Cycles*, *25*(3), 1–19. doi: 10.1029/2010GB003827

Parekh, P., Joos, F., & Müller, S. A. (2008). A modeling assessment of the interplay between aeolian iron fluxes and iron-binding ligands in controlling carbon dioxide fluctuations during Antarctic warm events. *Paleoceanography*, *23*(4), PA4202. doi: 10.1029/2007PA001531

Paulmier, A., Kriest, I., & Oschlies, A. (2009). Stoichiometries of remineralisation and denitrification in global biogeochemical ocean models. *Biogeosciences*, *6*(5), 923–935. Retrieved from https://bg.copernicus.org/articles/6/923/2009/ doi: 10.5194/bg-6-923-2009

Peterson, C. D., & Lisiecki, L. E. (2018). Deglacial carbon cycle changes observed in a compilation of 127 benthic d13C time series (20-6 ka). *Climate of the Past*, *14*(8), 1229–1252. doi: 10.5194/cp-14-1229-2018

Peterson, C. D., Lisiecki, L. E., & Stern, J. V. (2014). Deglacial whole-ocean d13C change estimated from 480 benthic foraminiferal records. *Paleoceanography*, *29*, 549–563. doi: 10.1002/2013PA002552.Received

Peterson, L. C., & Prell, W. L. (1985). Carbonate Preservation and Rates of Climatic Change: An 800 kyr Record from the Indian Ocean. In *The Carbon Cycle and Atmospheric CO$_2$: Natural Variations Archean to Present* (p. 251-269). American Geophysical Union (AGU). Retrieved from https://agupubs.onlinelibrary.wiley.com/doi/abs/10.1029/GM032p0251 doi: https://doi.org/10.1029/GM032p0251

Popp, B. N., Takigiku, R., Hayes, J. M., Louda, J. W., & Baker, E. W. (1989). The post-Paleozoic chronology and mechanism of 13 C depletion in primary marine organic matter. *American Journal of Science*, *289*(4), 436–454. Retrieved from https://www.ajsonline.org/content/289/4/436 doi: 10.2475/ajs.289.4.436

Ramirez, A. J., & Rose, A. W. (1992). Analytical geochemistry of organic phosphorus and its correlation with organic carbon in marine and fluvial sediments and soils. *American Journal of Science*, *292*(6), 421–454. Retrieved from https://www.ajsonline.org/content/292/6/421 doi: 10.2475/ajs.292.6.421

Raymo, M. E., Oppo, D. W., & Curry, W. (1997). The mid-Pleistocene climate transition: A deep sea carbon isotopic perspective. *Paleoceanography*, *12*(4), 546–559. doi: 10.1029/97PA01019

Regnier, P., Friedlingstein, P., Ciais, P., Mackenzie, F. T., Gruber, N., Janssens, I. A., ... Thullner, M. (2013). Anthropogenic perturbation of the carbon fluxes from land to ocean. *Nature Geoscience*, *6*(8), 597-607. doi: 10.1038/NGEO1830

Ridgwell, A., & Zeebe, R. (2005). The role of the global carbonate cycle in the regulation and evolution of the Earth system. *Earth and Planetary Science Letters*, *234*(3-4), 299-315. doi: 10.1016/j.epsl.2005.03.006

Ritz, S., Stocker, T. F., & Joos, F. (2011). A Coupled Dynamical Ocean-Energy Balance Atmosphere Model for Paleoclimate Studies. *Journal of Climate*, *24*, 349–375. doi: 10.1175/2010JCLI3351.1

Roth, R., & Joos, F. (2012). Model limits on the role of volcanic carbon emissions in regulating glacial-interglacial CO_2 variations. *Earth and Planetary Science Letters*, *329-330*, 141–149. doi: 10.1016/j.epsl.2012.02.019

Roth, R., Ritz, S. P., & Joos, F. (2014). Burial-nutrient feedbacks amplify the sensitivity of atmospheric carbon dioxide to changes in organic matter remineralisation. *Earth System Dynamics*, *5*(2), 321–343. doi: 10.5194/esd-5-321-2014

Rugenstein, J. K. C., Ibarra, D. E., & von Blanckenburg, F. (2019). Neogene cooling driven by land surface reactivity rather than increased weathering fluxes. *Nature*, *571*(7763), 99+. doi: {10.1038/s41586-019-1332-y}

Sarmiento, J. L., & Gruber, N. (2006). *Ocean Biogeochemical Dynamics*. Princeton: Princeton University Press.

Sarmiento, J. L., Orr, J. C., & Siegenthaler, U. (1992). A perturbation simulation of CO_2 uptake in an ocean general circulation model. *Journal of Geophysical Research: Oceans*, *97*(C3), 3621–3645. doi: 10.1029/91JC02849

Schmitt, J., Schneider, R., Elsig, J., Leuenberger, D., Lourantou, a., Chappellaz, J., ... Fischer, H. (2012). Carbon Isotope Constraints on the Deglacial CO_2 Rise from Ice Cores. *Science*, *336*(6082), 711–714. doi: 10.1126/science.1217161

Schmittner, A., Gruber, N., Mix, A. C., Key, R. M., Tagliabue, A., & Westberry, T. (2013). Biology and air–sea gas exchange controls on the distribution of carbon isotope ratios (d13C) in the ocean. *Biogeosciences*, *10*, 5793–5816. doi: 10.5194/bg-10-5793-2013

Schneider, R., Schmitt, J., Köhler, P., Joos, F., & Fischer, H. (2013). A reconstruction of atmospheric carbon dioxide and its stable carbon isotopic composition from the penultimate glacial maximum to the last glacial inception. *Climate of the Past*, *9*(6), 2507–2523. doi: 10.5194/cp-9-2507-2013

Schrag, D. P., Higgins, J. A., Macdonald, F. A., & Johnston, D. T. (2013). Authigenic Carbonate and the History of the Global Carbon Cycle. *Science*, *339*(6119), 540-543. Retrieved from https://www.science.org/doi/abs/10.1126/science.1229578 doi: 10.1126/science.1229578

Siegenthaler, U., & Muennich, K. O. (1981). Carbon-13/carbon-12 fractionation during carbon dioxide transfer from air to sea. In B. Bolin (Ed.), *Scope 16: Carbon cycle modelling* (pp. 249–257). Chichester: Wiley.

Siegenthaler, U., & Oeschger, H. (1987). Biospheric CO_2 emissions during the past 200 years reconstructed by deconvolution of ice core data. *Tellus B: Chemical and Physical Meteorology*, *39*(1-2), 140–154. doi: 10.3402/tellusb.v39i1-2.15331

Siegenthaler, U., Stocker, T. F., Monnin, E., Lüthi, D., Schwander, J., Stauffer, B., ... Jouzel, J. (2005). Stable Carbon Cycle-Climate Relationship During the Late Pleistocene. *Science*, *310*, 1313–1317.

Sigman, D. M., & Boyle, E. A. (2000). Glacial/Interglacial Variations In Atmospheric Carbon Dioxide. *Nature*, *407*(6806), 859–869. doi: 10.1038/35038000

Sigman, D. M., Hain, M. P., & Haug, G. H. (2010). The polar ocean and glacial cycles in atmospheric CO_2 concentration. *Nature*, *466*(7302), 47–55. doi: 10.1038/nature09149

Sigman, D. M., McCorkle, D. C., & Martin, W. R. (1998). The calcite lysocline as a constraint on glacial/interglacial low-latitude production changes. *Global Biogeochemical Cycles*, *12*(3), 409–427. doi: 10.1029/98GB01184

Stolper, D. A., Bender, M. L., Dreyfus, G. B., Yan, Y., & Higgins, J. A. (2016). A Pleistocene ice core record of atmospheric O_2 concentrations. *Science*, *353*(6306), 1427–1430. doi: 10.1126/science.aaf5445

Strassmann, K. M., & Joos, F. (2018). The Bern Simple Climate Model (BernSCM) v1.0: an extensible and fully documented open-source re-implementation of the

Bern reduced-form model for global carbon cycle-climate simulations. *Geoscientific Model Development*, *11*(5), 1887-1908. doi: 10.5194/gmd-11-1887-2018

Suchet, P., & Probst, J. (1995). A global-model for present day atmospheric soil CO_2 consumption by chemical erosion of continental rocks (GEM-CO2). *Tellus Series B - Chemical and Physical Meteorology*, *47*(1-2), 273-280. (4th Atmospheric CO(2) International Conference, CARQUEIRANNE, FRANCE, SEP 13-17, 1993) doi: 10.1034/j.1600-0889.47.issue1.23.x

Thompson, M., & Randerson, J. (1999). Impulse response functions of terrestrial carbon cycle models: method and application. *Global Change Biology*, *5*(4), 371-394. doi: 10.1046/j.1365-2486.1999.00235.x

Tréguer, P. J., Sutton, J. N., Brzezinski, M., Charette, M. A., Devries, T., Dutkiewicz, S., ... Rouxel, O. (2021). Reviews and syntheses: The biogeochemical cycle of silicon in the modern ocean. *Biogeosciences*, *18*(4), 1269–1289. Retrieved from `https://bg.copernicus.org/articles/18/1269/2021/` doi: 10.5194/bg-18-1269-2021

Tschumi, T., Joos, F., Gehlen, M., & Heinze, C. (2011). Deep ocean ventilation, carbon isotopes, marine sedimentation and the deglacial CO_2 rise. *Climate of the Past*, *7*(3), 771–800. doi: 10.5194/cp-7-771-2011

Van Cappellen, P., & Ingall, E. D. (1994). Benthic phosphorus regeneration, net primary production, and ocean anoxia: A model of the coupled marine biogeochemical cycles of carbon and phosphorus. *Paleoceanography*, *9*(5), 677–692. Retrieved from `http://doi.wiley.com/10.1029/94PA01455` doi: 10.1029/94PA01455

Walker, J. C. G., Hays, P. B., & Kasting, J. F. (1981). A negative feedback mechanism for the long-term stabilization of Earth's surface temperature. *Journal of Geophysical Research: Oceans*, *86*(C10), 9776-9782. Retrieved from `https://agupubs.onlinelibrary.wiley.com/doi/abs/10.1029/JC086iC10p09776` doi: https://doi.org/10.1029/JC086iC10p09776

Wallmann, K. (2010). Phosphorus imbalance in the global ocean? *Global Biogeochemical Cycles*, *24*(4), GB4030. Retrieved from `http://doi.wiley.com/10.1029/2009GB003643` doi: 10.1029/2009GB003643

Wallmann, K. (2014). Is late Quaternary climate change governed by self-sustained oscillations in atmospheric CO_2? *Geochimica et Cosmochimica Acta*, *132*, 413–439. doi: 10.1016/j.gca.2013.10.046

Wallmann, K., Schneider, B., & Sarnthein, M. (2016). Effects of eustatic sea-level change, ocean dynamics, and nutrient utilization on atmospheric pco_2 and seawater composition over the last 130 000 years: a model study. *Climate of the Past*, *12*(2), 339–375. Retrieved from `https://cp.copernicus.org/articles/12/339/2016/` doi: 10.5194/cp-12-339-2016

Wanninkhof, R. (2014). Relationship between wind speed and gas exchange over the ocean revisited. *Limnology and Oceanography: Methods*, *12*(6), 351–362. doi: 10.4319/lom.2014.12.351

Watson, B. A. J. (2016). Oceans on the edge of anoxia. *Science*, *354*(6319), 1529–1530.

Willeit, M., Ganopolski, A., Calov, R., & Brovkin, V. (2019). Mid-Pleistocene transition in glacial cycles explained by declining CO_2 and regolith removal. *Science Advances*, *5*(4). doi: 10.1126/sciadv.aav7337

Willeit, M., Ganopolski, A., Robinson, A., & Edwards, N. R. (2022). The Earth system model CLIMBER-X v1.0 – Part 1: Climate model description and validation. *Geoscientific Model Development*, *15*(14), 5905–5948. Retrieved from `https://gmd.copernicus.org/articles/15/5905/2022/` doi: 10.5194/gmd-15-5905-2022